A process-based framework for regional landslide debris inundation hazard assessment: application to the West Coast region of New Zealand

Kerry Leith, kerry.leith@earthsciences.nz, Earth Sciences New Zealand, 5011 Lower Hutt, New Zealand

Chris Massey, chris.massey@earthsciences.nz, Earth Sciences New Zealand, 5011 Lower Hutt, New Zealand

Biljana Lukovic, biljana.lukovic@earthsciences.nz, Earth Sciences New Zealand, 5011 Lower Hutt, New Zealand

Volker Wichmann, wichmann@laserdata.at, Laserdata GmbH, 6020 Innsbruck, Austria

This is a non-peer reviewed preprint submitted to EarthArXiv

A process-based framework for regional landslide debris inundation hazard assessment: application to the West Coast region of New Zealand

Kerry Leith[1], Chris Massey[1], Biljana Lukovic[1], Volker Wichmann[2]
[1]Earth Sciences New Zealand, 5011 Lower Hutt, New Zealand
[2]Laserdata GmbH, 6020 Innsbruck, Austria

Correspondence to: Kerry Leith (kerry.leith@earthsciences.nz)

Abstract. Regional landslide debris inundation hazard assessments commonly rely on scenario-based formulations that require explicit enumeration of discrete landslide events. While effective for local studies, these approaches are computationally intensive, sensitive to scenario design choices, and difficult to apply consistently at regional scales where landslide catalogues are incomplete and long-term behaviour is poorly constrained. In parallel, geomorphological models provide insight into landslide-driven sediment production over long timescales, but are rarely formulated to generate spatially explicit hazard metrics relevant to runout and inundation.

Here we present the Landslide Source-to-Inundation Process Model (LS-IPM), a reduced-complexity, process-based framework that reframes landslide debris inundation hazard as a flux-based intensity problem. Rather than simulating discrete landslide scenarios, LS-IPM couples spatially distributed landslide sediment production to mass-conservative, topography-controlled debris routing, producing continuous fields of landslide-derived debris flux. Landslide magnitude and frequency are implicitly linked through a constraint on sediment production, allowing hazard to be evaluated everywhere in the landscape without explicit specification of individual failure events.

We apply the LS-IPM to the ~25,000 km^2 West Coast region of New Zealand at 25 m resolution, generating hazard estimates for present-day conditions, future climate scenarios (RCP6, 2081–2100), and a scenario Alpine Fault Mw 8.0 earthquake. Results show highest debris flux on steep slopes, at the base of high-relief landforms, and along convergent topography, consistent with geomorphological expectations. Approximately 80 % of the region is affected by some degree of landslide debris inundation hazard, with future climate conditions expected to increase mean annual debris flux by ~50%.

By integrating geomorphological constraints with reduced-complexity runout modelling, the LS-IPM provides a scalable framework for regional landslide debris inundation hazard assessment that is compatible with subsequent probabilistic risk analysis.

1 Introduction

Landslides are a dominant geomorphic and hazardous process in steep terrain, exerting strong controls on hillslope form, sediment supply to river networks, and the distribution of damage and loss during extreme events. For hazard assessment, a central difficulty lies in linking where landslides are likely to originate, how much material they produce, and how that material is redistributed downslope, particularly at regional scales where individual failures cannot be predicted deterministically. While landslide susceptibility and triggering are increasingly well constrained through empirical and physically based approaches, translating landslide occurrence into spatially continuous measures of downslope or downstream hazard remains challenging.

In this study, we present a new methodology for landslide hazard assessment, suitable for regional hazard assessment and subsequent risk analysis across an approximate 25,000 km^2 region of the West Coast of the South Island of New Zealand. The West Coast is the country's wettest region, receiving over 6 m of annual rainfall in some locations, and lies along the active Pacific - Australian plate boundary, where there is a 75 % probability of rupture on the Alpine Fault in the next 50 years, and an 80% probability this will result in a Mw 8.0 earthquake. High uplift and erosion rates (>10 mm/yr) are matched by high rates of landsliding (in this study, we demonstrate that approximately 80% of the land area is susceptible to landslide debris inundation), and data suggest the western Southern Alps are in dynamic equilibrium, with landslides the dominant erosional process.

1.1 Approaches to landslide runout and hazard modelling

Landslide runout and debris inundation hazard models span a range of formulations and levels of process representation (Keck et al., 2024). At one end of this range are empirical and statistical site-specific models, which estimate runout extent using simple geometric or kinematic rules based on an estimate of landslide source properties (e.g. Lin et al., 2025; Reid et al., 2016). These approaches are computationally efficient and widely applied, but typically represent runout as a static footprint derived from observed volume–distance or reach-angle relationships, without explicitly representing transport or deposition processes.

At the other end of the range are continuum-based mechanistic models, which conceptualise landslide runout as a single- or multi-phase flow and solve depth-integrated forms of the Navier–Stokes equations for incompressible, free-surface motion (Frank et al., 2015; Han et al., 2015; Iverson and Denlinger, 2001; Medina et al., 2008; Pudasaini and Krautblatter, 2021). Such models are capable of simulating time-dependent flow behaviour, velocities, and flow depths, but often require prior specification of the total mobilised volume and extensive parameterisation, which can limit their application at regional scales (Barnhart et al., 2021; Han et al., 2015).

Between these extremes lie reduced- or appropriate-complexity flow-routing models, which abstract the dominant physical controls on landslide movement into simplified, rule-based representations while retaining explicit dependence on topography and mass conservation (e.g. Murray, 2007). These models typically operate on gridded terrain, require the initial landslide location and volume as primary inputs, and approximate runout and deposition using parameterised routing and stopping rules (Aaron, 2023; Clerici and Perego, 2000; Goetz et al., 2021; Gorr et al., 2022; Guthrie and Befus, 2021; Han et al., 2017, 2021; Horton et al., 2013; Keck et al., 2024; Liu et al., 2022; McDougall, 2017). Their reduced computational cost makes them suitable for regional hazard applications, although their performance can depend on site-specific parameterisation. A related class of hybrid approaches combines elements of mechanistic formulations (e.g. Frank et al., 2015) with empirical or reduced-complexity representations in order to balance physical realism and computational efficiency (D'Ambrosio et al., 2003; Iovine et al., 2005; Lancaster et al., 2003; McDougall and Hungr, 2004; de Vilder et al., 2022).

1.2 Landslides in regional risk assessment

At regional scale, landslide hazard modelling typically proceeds in two conceptual steps: (i) estimation of landslide source occurrence or susceptibility, often conditioned on a triggering mechanism, and (ii) estimation of downslope impact through runout or inundation modelling. Susceptibility models most commonly identify areas where landslides are more likely to initiate, but by themselves do not quantify downstream effects. Runout models, in turn, require assumptions about source locations, volumes, and failure timing, which are often poorly constrained and highly uncertain at large spatial extents.

To manage this uncertainty, many applied studies adopt representative scenarios or characteristic landslide sizes (Barnhart et al., 2026; Bera et al., 2021; Keck et al., 2024; Pollock et al., 2019; Pollock and Wartman, 2025, 2026; Santangelo et al., 2021; de Vilder et al., 2022), consistent with more traditional site-specific hazard and risk assessments. While pragmatic, this approach introduces a structural mismatch between the discrete nature of landslide occurrence and the continuous representation of impact probability, particularly when results are aggregated to regional or annualised hazard or risk metrics. As a result, regional hazard estimates may depend as much on scenario design choices (e.g. the location and characteristics of simulated landslides) as on underlying geomorphic controls.

1.3 Landslides in landscape evolution models

In parallel with hazard-oriented modelling, the geomorphology community has developed landscape evolution models (LEMs) that explicitly represent landslides as a mechanism of sediment production and topographic adjustment within coupled hillslope–fluvial systems. A prominent example is HyLands (Campforts et al., 2020), a hybrid landscape evolution model implemented within the TopoToolbox Landscape Evolution Model (TTLEM) framework (Campforts et al., 2017). HyLands integrates stochastic landslide erosion with fluvial incision and sediment transport, allowing landslide-derived sediment to interact dynamically with river processes through time. Landslides are represented as episodic mass-wasting events governed by stability criteria and depth limits. The resulting sediment is routed, deposited, and potentially re-entrained within a mass-conservative sediment-routing scheme. The primary objective of HyLands is to explore how landsliding influences long-term landscape morphology, sediment budgets, and the coupling between hillslopes and channels, rather than to generate event-scale hazard metrics.

Closely related conceptual approaches have been developed within the Landlab modelling framework (Hutton et al., 2020), which provides a modular, open-source platform for landscape evolution modelling. Several Landlab components represent landslides or threshold hillslope failure as stochastic or rule-based mass-removal processes, coupled to fluvial incision and sediment transport models (see Keck et al., 2024 and references therein). These implementations similarly treat landslides as sources of sediment flux that contribute to landscape-scale erosion and deposition over long timescales, often using simplified stability thresholds, depth limits, and instantaneous mass redistribution. As with HyLands, the emphasis in Landlab-based landslide modules is on understanding emergent landscape behaviour, sediment connectivity, and feedbacks between hillslope processes and channel dynamics, rather than on predicting the spatial extent or intensity of debris inundation for specific hazardous events.

HyLands and Landlab-based models share two conceptual elements that are directly relevant to hazard modelling. First, landslides are framed as spatially distributed sediment sources whose impacts accumulate through time, rather than as isolated events requiring explicit enumeration. Second, downstream effects are mediated by transport efficiency and connectivity, such that only a subset of landslide-derived sediment contributes to channelised transport or distal deposition. Recent developments within the Landlab framework have extended these concepts toward hazard-oriented applications. In particular, the MassWastingRunout component of Keck et al. (2024) provides a reduced-complexity, rule-based representation of landslide runout that can be used both within landscape evolution simulations and for regional landslide hazard assessment.

1.4 Reduced-complexity regional hazard modelling approaches

Reduced-complexity, grid-based models have been increasingly used to represent landslide runout and debris inundation at regional scales, where fully dynamic simulations are impractical. The MassWastingRunout (MWR) component of the Landlab modelling framework (Keck et al., 2024) is a rule-based landslide runout model in which landslide runout is represented through repeated, parameterised runout realisations propagated downslope from specified source areas using topography-driven routing and mass-conservative deposition rules. Uncertainty in landslide size, mobility, and routing parameters is incorporated through probabilistic sampling, and hazard is quantified by aggregating multiple realisations of runout from prescribed source areas. In this formulation, landslide hazard is expressed in terms of the spatial frequency or probability of runout occurrence at a given location, derived from ensembles of discrete event footprints.

The Landslide Source-to-Inundation Process Model (LS-IPM) framework presented here adopts a similar level of process abstraction and computational complexity, but differs in how landslide activity and downslope impacts are represented. Rather than simulating ensembles of individual landslide events, the LS-IPM treats landsliding as a spatially distributed sediment-production process acting on a fixed landscape. Landslide debris is generated at source areas according to expected production rates and triggering likelihoods, and is routed downslope using mass-conservative, rule-based gravitational transport consistent with regional-scale modelling. Model outputs are expressed as landslide-derived debris flux, representing the expected rate at which landslide material passes through, or accumulates at a location.

1.5 Motivation for the Landslide Source-to-Inundation Process Model (LS-IPM)

Development of the LS-IPM was motivated by the need for a scalable, spatially continuous representation of landslide debris inundation hazard that does not require high-resolution event-based landslide catalogues, or rely on user-defined enumeration of individual landslide scenarios. The LS-IPM addresses this by expressing hazard magnitude directly as landslide debris flux, derived from the expected rate of landslide sediment production and its redistribution downslope using empirically constrained gravitational process routing. This flux-based formulation allows hazard to be evaluated everywhere in the domain, including locations affected by numerous small, or infrequent but large landslides, without requiring explicit specification of which slopes fail in any single event.

Accordingly, the LS-IPM approach differs from previous reduced-complexity models primarily in its aggregation of hazard, rather than in the underlying treatment of downslope transport. In Keck et al. (2024), for example, hazard emerges from the accumulation of probabilistic runout footprints associated with discrete landslide events. In the LS-IPM, hazard intensity is represented by the long-term or event-integrated debris flux arising from all potential sources, measured either as an annualised quantity (m^3 m^{-2} yr^{-1}) or as an event-integrated quantity (m^3 m^{-2} $event^{-1}$). Under this formulation landslide volume distributions, and susceptibility to triggers are derived from landslide catalogue data, though hazard is ultimately constrained by the rate at which landslide debris is generated and redistributed through the landscape. Landslide occurrence frequency is therefore not treated as an independent variable; instead, it is implicitly constrained by the volume of material mobilised. A greater contribution from large landslides necessarily implies a lower frequency of occurrence in order to adhere to a physically plausible debris-production rate.

The LS-IPM also contrasts with hybrid empirical runout-envelope methods and probabilistic aggregations of runout realisations, in which model inputs are typically derived from a frequentist interpretation of landslide occurrence (Lee and Jones, 2023). In such approaches, historical landslide inventories are used to estimate the expected number of discrete landslide or runout events of a given size within a specified area and time window (e.g. de Vilder et al., 2022). While uncertainty may be incorporated through sampling of landslide size, mobility, or routing parameters, hazard remains scenario-based and frequency is inferred directly from past event counts. Debris production is rarely treated as a limiting constraint, and hazard is expressed primarily in terms of the likelihood of discrete impacts rather than as a rate-limited flux of material through the landscape.

As the LS-IPM does not require explicit enumeration of landslide scenarios, it avoids a key structural limitation common to many reduced-complexity and probabilistic runout approaches (e.g. Keck et al., 2024; de Vilder et al., 2022). In scenario-based frameworks, hazard estimates depend on user-defined choices regarding the number, size, and spatial distribution of discrete landslide events used to represent long-term behaviour. At regional scales, where landslide occurrence is spatially heterogeneous and individual failures cannot be predicted deterministically, these design choices can exert a first-order control on predicted hazard, independent of underlying geomorphic or geological constraints.

By formulating landslide hazard in terms of debris flux, the LS-IPM instead enforces consistency between landslide magnitude and frequency through an explicit rate constraint on sediment production. Hazard intensity emerges from the integrated contribution of all feasible landslide sources and volumes, rather than from the aggregation of a finite set of hypothetical events. This removes the need to prescribe how many landslides of a given size "should" occur within a given time window, and ensures that regional hazard estimates remain physically plausible even where historical inventories are sparse, incomplete, or non-representative of long-term behaviour.

The resulting framework is therefore particularly well suited to regional hazard assessment, where the objective is not to predict individual landslide occurrences, but to quantify the spatial distribution of potential debris inundation conditioned on geomorphic process rates and present-day landscape structure. In this context, LS-IPM provides a computationally efficient means of translating landslide susceptibility and sediment production into spatially continuous hazard intensity metrics that are directly comparable across regions, scenarios, and planning time horizons.

2 Methodology Overview

2.1 Consideration of hazard and risk

Landslide hazard within the LS-IPM framework is quantified through a coupled workflow comprising three components, namely the:

1. Landslide Source Susceptibility model (LSS),
2. Landslide Sediment Production model (LSP), and
3. Landslide Sediment Distribution model (LSD).

The LSS model describes the probability of slope failure for either mean-annual or scenario-based triggering conditions. The LSP component estimates the volume of debris generated from all kinematically feasible landslides, informed by long-term erosion rates and observed landslide size distributions. The LSD model simulates downslope debris transport using reduced-complexity, mass-conservative routing rules to estimate the spatial distribution of landslide-debris flux.

In this framework, landslide hazard is quantified in terms of landslide-debris flux, which integrates both the frequency and magnitude of all potential landslides capable of affecting a given location. This metric reflects the cumulative influence of landslide sediment production upslope and the capacity for that sediment to be transported through the landscape.

The landslide-debris flux metric therefore provides a measure of hazard intensity but does not, by itself, constitute a measure of risk, which requires explicit separation of frequency, intensity, exposure, and vulnerability. Intermediate outputs of the LSD model are used in Part 2 of this study to calculate the Probability of Inundation (P_i) and associated risk metrics, including Annual Property Loss Risk (APLR) (Leith and Wichmann, 2026).

2.2 Landslide Source-Susceptibility (LSS) Model

The LSS model is used to evaluate the relative probability of a landslide originating from a given location (termed here 'occurring') as a result of a given trigger (e.g. rainfall or earthquake) and associated return interval. The model assumes that all landslides occurring at a given location are the result of some trigger, and calculates the annual probability of failure by integrating outputs from landslide source-susceptibility models, trained using catalogues of landslides triggered by discrete events.

In order to calculate the total annual probability of a landslide occurring ($P_{(x,y)}$), we combine rainfall-induced landslide susceptibility (S_{RIL}) and earthquake-induced landslide (S_{EIL}) susceptibilities over the return-period bands represented by each model. For each trigger type, the susceptibility model probability that a grid cell is affected by a landslide source during the representative trigger event with return period (T_i). This event susceptibility is converted to a mean annual probability by multiplying it by the annual frequency of the corresponding return-period band, where (T_{min}) and (T_{max}) are the lower and upper bounds of the return-period band represented by T_i. These bounds are defined as the midpoints between adjacent representative trigger return periods (see Eq's (1)and (2)).

To convert from the probability of a grid cell containing a landslide source to the expected fractional area of landslide source within the cell, the event probabilities are multiplied by the ratio of the geometric-mean landslide source area for the relevant trigger type, ($\overline{A_{L(T)}}$), to the model grid-cell area, (A_T), where (T) denotes the trigger type on which the susceptibility model is trained. The derivation of ($\overline{A_{L(T)}}$) for the West Coast region is described in (Leith et al., 2025b).

Equations 1 and 2 describe the mean annual fractional source-area occupancy associated with rainfall-induced (P_{RIL}) and earthquake-induced landslides, respectively (P_{EIL}). The total annual probability of failure is described in Eq. 3:

$$P_{RIL(x,y)} = \sum_i S_{RIL,i(x,y)} \left(\frac{1}{T_{min,i}} - \frac{1}{T_{max,i}}\right) \times min\left(\frac{\overline{A_{L,RIL,i}}}{A_{RIL}}, 1\right) \tag{1}$$

$$P_{EIL(x,y)} = \sum_i S_{EIL,i(x,y)} \left(\frac{1}{T_{min,i}} - \frac{1}{T_{max,i}}\right) \times min\left(\frac{\overline{A_{L,EIL,i}}}{A_{EIL}}, 1\right) \tag{2}$$

$$P_{(x,y)} = P_{RIL(x,y)} + P_{EIL(x,y)} \tag{3}$$

The LSS model output therefore represents the expected annual fraction of each grid cell occupied by landslide source area due to rainfall- and earthquake-induced landsliding. Expressed as $m^2\ m^{-2}\ kyr^{-1}$ (per thousand years), a value of 0.5 kyr^{-1} indicates that either 50% of the grid cell is expected to be occupied by a landslide source within a 1000-year period, or, alternatively, the entire area is expected to be associated with a landslide source over a 2000-year period. Although only earthquake, and rainfall triggers are considered here, additional triggers can be included, as the annual probability of failure is simply considered the sum of all probabilities (see Eq. 3).

2.3 Landslide Sediment-Production (LSP) Model

The Landslide Sediment-Production (LSP) model provides the mass-balance constraint that links landslide source susceptibility to debris runout within the LS-IPM. Rather than prescribing the number of landslides of different sizes that occur within a given period, the model begins with an estimate of the rate at which landslide-derived sediment can be generated from the landscape. This sediment supply is subsequently distributed among landslide triggers and source-volume classes according to the relative probabilities derived from the LSS model and the range of landslide sizes that can feasibly originate from each location.

Landsliding is a major contributor to erosion and sediment transfer in steep landscapes and may exert a first-order control on long-term denudation rates (Burbank et al., 1996; Larsen and Montgomery, 2012; Montgomery and Brandon, 2002). The LSP model uses this relationship in three steps: estimation of the landslide-derived sediment supply, identification of the landslide volumes that are geometrically and mechanically feasible at each location, and partitioning of the available sediment among those feasible volume classes. This formulation means that landslide magnitude and frequency are not treated as independent inputs. For a fixed rate of sediment production, allocating a greater proportion of material to large landslides necessarily implies that such failures occur less frequently than smaller landslides. The LSP model therefore provides the link between long-term geomorphic rates and the discrete landslide-volume classes required by the runout model.

2.3.1 Landslide sediment-production rate

We represent the long-term supply of landslide debris independently from the frequency of individual landslide events. Let ($\dot{E}_{(x,y)}$) describe the mean erosion rate at a location, and let (ω_L) represent the proportion of that erosion attributable to landsliding. Because material mobilised by slope failure generally occupies a greater volume than the equivalent in-situ material, a bulking factor (η_L) is also applied. The resulting mean rate of landslide sediment production is:

$$\dot{E}_{L(x,y)} = \dot{E}_{(x,y)} \times \omega_L \times \eta_L \tag{4}$$

Here ($\dot{E}_{L(x,y)}$) represents the volume-equivalent thickness of landslide debris generated per unit area and time. It is therefore a sediment-supply rate rather than an estimate of the occurrence frequency of individual failures.

Spatially distributed erosion-rate datasets provide one means of constraining ($\dot{E}_{(x,y)}$) over large areas (e.g. Dymond et al., 2010; Hicks et al., 2011, 2019; Roda-Boluda et al., 2023). Their use allows the long-term landslide sediment budget to be constrained independently of the duration or completeness of mapped landslide inventories. Alternative methods to constrain $\dot{E}_{L(x,y)}$ may include mechanistic weathering, fracturing, and soil production models (e.g. Eppes et al., 2020; Eppes and Keanini, 2017), global statistical datasets comparing climate, vegetation, and / or topographic metrics (e.g. Mishra et al., 2019; Schaller and Ehlers, 2022), or long-term observational records (e.g. sediment removal from transport routes).

The regional erosion dataset, values of (ω_L) and (η_L), and other case-study-specific assumptions adopted for the West Coast implementation are described in Sect. 3.2.1. Adjustments to sediment production for future-climate and individual triggering scenarios are described in Sect. 2.5.

2.3.2 Kinematic constraint on landslide source volume

The sediment-production constraint determines how much material is available, but not the size of individual landslides that can originate from a given part of the landscape. The LSP model therefore uses a kinematic source model to define an upper bound on feasible source volume at each location.

This is a regional screening model rather than a slope-stability calculation. It does not explicitly solve the balance between driving and resisting forces and is not intended to reproduce individual failure surfaces. Instead, it identifies the source sizes that can reasonably be accommodated by the available topographic relief while maintaining approximate relationships between landslide area, volume and material strength. The approach is conceptually related to other methods for estimating potential landslide source geometry and volume models (see Jaboyedoff et al., 2020; Pollock and Wartman, 2025; Prajapati and Jaboyedoff, 2022 and references therein), but combines topographic and material-strength constraints.

Potential failure units are first identified from the amount of topography lying above a reference surface defined by a threshold basal angle (θ_{XST}), following the concept of excess topography (Blöthe et al., 2015). The calculation is undertaken over a neighbourhood large enough to encompass the maximum landslide size represented by the model. Intersections between the resulting limiting surfaces define contiguous terrain units within which sufficiently large source geometries may be accommodated. Small isolated boundaries are removed where they would artificially subdivide these units at scales below the largest modelled source (see Leith et al., 2025b for further details of this calculation).

Within each unit, the available horizontal distance to the unit boundary provides a spatial constraint on potential landslide dimensions. This geometric constraint is combined with the commonly observed power-law relationship between landslide source area (A) and volume (V):

$$V = \alpha A^{\gamma} \tag{5}$$

Area-volume scaling has been documented across a wide range of landslide types, magnitudes and settings, although it is best constrained for landslides below approximately 10^6 m^3 (Guzzetti et al., 2009; Jones et al., 2025; Larsen et al., 2010; Massey et al., 2020b). Observations commonly indicate (γ) values of approximately 1.4, with published estimates generally between 1 and 1.5 (Guzzetti et al., 2009; Larsen et al., 2010; Massey et al., 2020c; Pollock, 2020).

Klar et al. (2011) developed analytical solutions based on mechanical controls on landslide geometry that allow the scaling coefficient (α) to be related to mechanical properties of the source material. For the adopted formulation,

$$\alpha = k \left(\frac{c}{\rho_{L\,(x,y)}} \right)^{d} \tag{6}$$

where (c) is representative cohesive strength, ($\rho_{L\,(x,y)}$) is material density, and assuming a generic 2D model in which landslide depth is proportional to the length of its source, k = 0.45, $d = 0.28$ and $\gamma = 1.36$ (Klar et al., 2011).

For each grid cell, the horizontal distance ($r_{(x,y)}$) to the nearest failure-unit boundary is used to define the largest representative source area that can be accommodated locally. Assuming a cylindrical representation of source volume, Eq. (5) can then be expressed as a limiting landslide depth:

$$D_{(x,y)} = \frac{V_{(x,y)}}{A_{(x,y)}} = \frac{\alpha \left(\pi\, {r_{(x,y)}}^{2}\right)^{\gamma}}{\pi\, {r_{(x,y)}}^{2}} \tag{7}$$

The resulting depth surface tapers towards the margins of each potential failure unit and increases where greater source dimensions can be accommodated.

Because local DEM roughness should not directly dictate the geometry of an idealised landslide scarp, the calculation is undertaken relative to a smooth envelope interpolated between the boundaries of each failure unit. The residual between this envelope and the original topography is then accounted for when deriving the limiting failure surface. The resulting geometry is not intended to represent a predicted landslide surface; its purpose is to preserve approximate area-volume scaling while identifying the largest source volumes that can reasonably be supported by the available relief.

A separate treatment is required for shallow failures that may occur on steep slopes but are not captured by the deeper excess-topography geometry. Cells exceeding the threshold surface gradient θ_{NAT} are therefore assigned at least the minimum landslide-depth class where they have not already been assigned a greater feasible depth. Together, these two constraints provide a spatially continuous estimate of the maximum source size available to the subsequent volume-partitioning calculation (see Figure 1; landslide area-volume scaling).

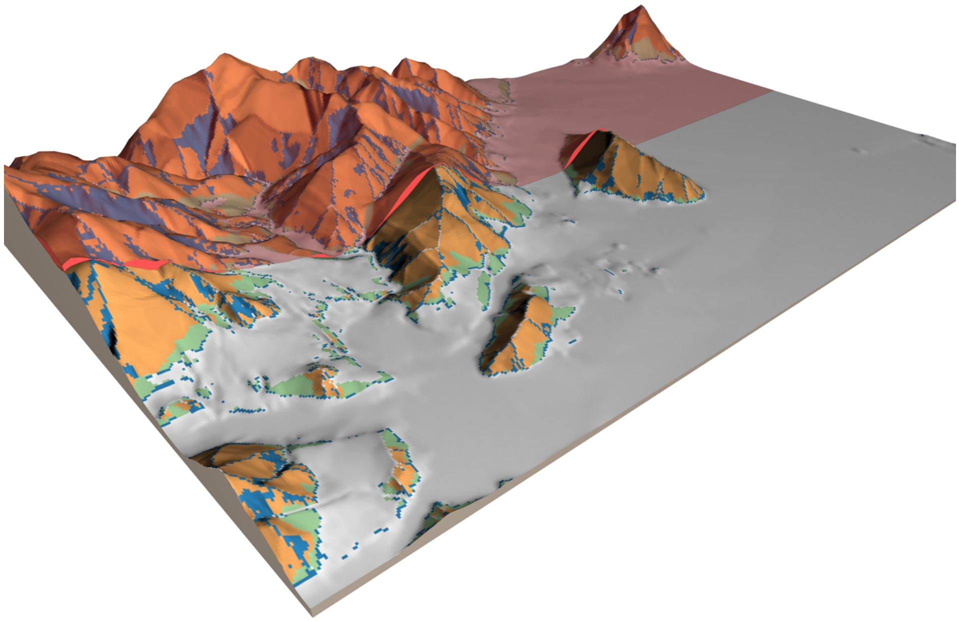

Figure 1: Example of the maximum depth surface derived from the kinematic landslide source model (foreground). Surface topography is superimposed in the red-shaded region for comparison (background). Green denotes the threshold slope angle for excess topography (θ_{XST}), orange denotes the landslide area-volume scaling [$D_{(x,y)}$] and blue denotes steep slopes otherwise not captured (θ_{NAT}). Reproduced from Leith et al. (2025b).

2.3.3 Characteristic landslide-volume distributions

The kinematic model provides an upper bound on landslide size, but does not determine how the available sediment should be divided among smaller failures. This is constrained using empirical landslide-volume distributions.

Landslide inventories from different environments commonly show characteristic frequency-volume distributions despite substantial differences in absolute landslide size and abundance. Brunetti et al. (2009) for example, found that measured landslide source volumes from multiple inventories could be approximated by log-normal distributions around characteristic geometric-mean volumes. Similar characteristic behaviour has subsequently been identified in other datasets (Jones et al., 2025; Medwedeff et al., 2020; Moreno et al., 2023). Within the LS-IPM, a trigger-specific log-normal volume distribution is therefore used to define the relative abundance of potential landslide sizes. Importantly, this distribution does not determine the total sediment production. It determines only how the sediment-production rate from Eq. (4) is distributed among the range of landslide volumes that are kinematically feasible at a given location. The method to enable this partitioning is discussed in the following section.

2.3.4 Partitioning sediment production across landslide volumes

The final stage of the LSP calculation partitions the sediment-production rate in Eq. (4) among landslide-volume classes, triggers and return-interval bands.

For each landslide-volume class, Eq. (5) is inverted to obtain the representative source area ($A_{L(c)}$):

$$A_{L(c)} = \sqrt[\gamma]{\frac{V_L}{\alpha}} \qquad (8)$$

where V_L is the landslide volume associated with class range c. The corresponding representative mean depth ($\overline{D}_{L(c)}$) is:

$$\overline{D}_{L(c)} = \frac{V_{L(cg)}}{A_{L(cg)}} \quad (9)$$

Where cg denotes the geometric mean of the volume class interval.

These characteristic depths are compared with the mean limiting depth derived from the kinematic source model. A binary feasibility term ($K_{L(c)(x,y)}$) is defined for each volume class, assuming landslides of a given class range can occur if the mean depth derived from the kinematic model ($\overline{D}_{\mathrm{K}(x,y)}$) is greater than the lower bounding volume of that depth class ($\overline{D}_{L(c)}$).

$$K_{L(c)(x,y)} = \begin{cases} 1, & \overline{D}_{K(x,y)} > \overline{D}_{L(c)} \\ 0, & otherwise, \end{cases} \quad (10)$$

The log-volume centre of the largest feasible class is described by $z_{max(x,y)}$, while the centre of the smallest modelled class is $z_{min(x,y)}$:

$$z_c = log_{10}\left(V_{L(cg)}\right) \quad (11)$$

The trigger-specific landslide-volume distribution is then truncated at this local upper-volume limit. We describe the likelihood of a landslide of a valid volume class occurring ($N_{(x,y)(T)}$) using the probability mass between the minimum and maximum represented log-volumes. This is described in Eqs. (12) and (13) below:

$$N_{(x,y)(T)} = F_T\left[z_{max(x,y)}\right] - F_T\left(z_{min(x,y)}\right) \quad (12)$$

where F_T is the normal CDF for trigger *T*. Written explicitly,

$$N_{(x,y)(T)} = \frac{1}{2}\left[erf\left(\frac{z_{max(x,y)} - V_{\mu(T)}}{V_{\sigma(T)}\sqrt{2}}\right) - erf\left(\frac{z_{min(x,y)} - V_{\mu(T)}}{V_{\sigma(T)}\sqrt{2}}\right)\right] \quad (13)$$

where $V_{\mu(T)}$ and $V_{\sigma(T)}$ describe the mean and standard deviation of the $\log_{10}$ landslide-volume distribution associated with trigger T. erf is a standard error function used in probability and statistics.

We account for increased proportionality of lower-volume landslides at locations in which the kinematic model suggests that larger landslides are infeasible by normalising the PDF by the cumulative distribution function up to the upper depth limit (assuming that lower volumes can occur at any feasible location). The the conditional probability density weight for class c ($N_{L(c)(T)(x,y)}$) is then given by a conditional formula in which proportions are either equal to the volume-range-normalised PDF (when the depth class is kinematically feasible) or set to zero:

$$N_{L(c)(T)(x,y)} = K_{L(c)(x,y)} \begin{cases} \dfrac{\frac{1}{V_{\sigma(T)}\sqrt{2\pi}} exp\left[-\frac{(z_c - V_{\mu(T)})^2}{2\,V_{\sigma(T)}{}^2}\right]}{N_{(x,y)(T)}} & if\ 0 \leq \overline{D}_{L(c)} \leq D_{(x,y)} \\ 0 & \end{cases} \quad (14)$$

In order to determine the proportion of erosion generated by each valid volume-class range ($\mathrm{D}_{L(c)(T)(x,y)}$), the probability of landsliding is calculated by integrating the likelihood of occurrence with respect to the breadth of the class range

$(\omega_{(c)} = log_{10}(V_{L(c)}) - log_{10}(V_{L(c-1)})$ and multiply by the mean erosional depth of the interval ($\overline{D}_{L(cg)}$), calculated by substituting $V_{L(cg)}$ into Eq. (9) and Eq. (10).

$$D_{L(c)(T)(x,y)} = N_{L(c)(T)(x,y)} \times \omega_{(c)} \times \overline{D}_{L(cg)} \qquad (15)$$

The resulting values are normalised across all feasible classes to give the fraction of landslide-derived erosion allocated to each volume class and trigger:

$$V_{L(c)(T)(x,y)} = \frac{D_{L(c)(T)(x,y)}}{\sum_{c_{min}}^{c_{max}} D_{L(c)(T)(x,y)}} \qquad (16)$$

Finally, the total sediment-production rate is divided among the trigger and return-interval combinations represented by the LSS model. For a given trigger T, return-interval band RI, and volume class c,

$$\dot{E}_{L(c)(T,RI)(x,y)} = \dot{E}_{L(x,y)} \times \frac{P_{(x,y)(T_{RI-1},T_{RI})} \times V_{L(c)(T)(x,y)}}{P_{(x,y)}} \qquad (17)$$

where $P_{(x,y)(T_{RI-1},T_{RI})}$ is the annual contribution from the relevant trigger and return-interval band and $P_{(x,y)}$ is the total annual landslide probability derived by the LSS model.

Equation (16) is the key coupling between the LSS and LSP components. The LSS model determines the relative allocation of sediment production among triggering conditions, while the kinematic and volume-distribution models determine its allocation among landslide sizes. Neither changes the total long-term sediment supply. Consequently, summing $\dot{E}_{L(c)(T,RI)(x,y)}$ over all feasible volume classes, triggers and return intervals recovers $\dot{E}_{L(x,y)}$. These spatially distributed sediment-production rates form the source inputs to the Landslide Sediment-Distribution model described in the following section.

2.4 Landslide Sediment-Distribution (LSD) Model

The Landslide Sediment-Distribution (LSD) model translates the spatially distributed sediment-production rates calculated by the LSP model into a measure of downslope landslide-debris flux. In doing so, it provides the final spatial component of the LS-IPM hazard calculation: the LSS model determines the relative likelihood of source activity, the LSP model constrains the volume of sediment generated, and the LSD model determines how that material is redistributed through the landscape.

Rather than attempting to reproduce the full dynamics of individual landslides, the LSD model represents the first-order controls on debris mobility using reduced-complexity routing. This is consistent with the regional-scale objective of the LS-IPM, for which the principal requirement is to determine where sediment from a spatially distributed population of potential landslide sources can travel, and how the contributions from those sources accumulate at downstream locations.

2.4.1 Gravitational Path Process (GPP) model

Debris transport is simulated using the Gravitational Path Process (GPP) model of Wichmann (2017). GPP is a grid-based modelling framework in which material released from source cells is propagated downslope according to topography, a stochastic routing algorithm and a prescribed representation of material mobility. Repeated routing iterations allow material originating from a single source cell to follow alternative downslope trajectories, thereby representing uncertainty and dispersion in potential landslide paths.

For each iteration, a fraction of the material assigned to the source cell is transported along the selected path. Material passing through a grid cell contributes to the accumulated flux at that location, while material deposited during the simulation is removed from the amount available for subsequent transport. The model can additionally modify the routing surface through deposition and sink filling, allowing progressive sediment accumulation to affect the passage of material through local depressions and depositional areas (Wichmann, 2017).

This formulation is particularly useful within the LS-IPM because the routing rules are applied to sediment packets rather than to explicitly defined individual landslide polygons. Sediment generated by multiple potential sub-grid failures can therefore be represented by the source loading of a grid cell and routed according to mobility rules appropriate to the corresponding landslide-volume class. The method consequently does not require each landslide contributing to long-term sediment production to be explicitly located or simulated as a discrete event.

2.4.2 Landslide-source loading

The source material supplied to each GPP simulation is taken directly from the LSP output for a particular combination of landslide-volume class c, trigger T, and return-interval range RI. Because these LSP outputs are expressed as sediment-production rates, they are converted to a source-material thickness by integrating over a period σ:

$$M_{GPP(c)(T,RI)(x,y)} = \dot{E}_{L(c)(T,RI)(x,y)} \times \sigma \qquad (18)$$

where $M_{GPP(c)(T,RI)(x,y)}$ is the thickness of source material supplied to the corresponding GPP simulation. The sediment-production rate is derived from Eq. (16).

The integration interval allows spatially distributed rates of sediment production to be represented as finite quantities of material during routing. This is necessary because deposition and sink filling operate on finite sediment volumes: material accumulated from multiple source locations can progressively fill depressions or contribute to depositional landforms before further material is routed downslope. The resulting routed flux is subsequently normalised by the same integration interval, so that annualised outputs retain their original temporal units.

The choice of σ is therefore primarily a modelling parameter controlling the amount of sediment present during a GPP simulation rather than an assumed recurrence interval for an individual landslide. Because deposition can modify subsequent routing, however, the calculation is not strictly independent of the selected value. The integration interval and its sensitivity are consequently treated as part of the case-study implementation described in Sect. 3.

2.4.3 Representation of landslide mobility

The LSD model represents two styles of landslide movement: avalanche-type and flow-type transport. These classifications are used to bracket characteristic differences in debris mobility rather than to reproduce the rheology of individual landslide types.

Avalanche-type movement is represented using the empirical energy-line, or fahrböschung, principle (Heim, 1932). In this formulation, the available gravitational potential energy progressively decreases as material moves downslope, with the limiting reach controlled by the adopted fahrböschung angle. Energy-line approaches have been widely used to estimate the runout of rapid gravitational mass movements (e.g. Corominas, 1996; Massey et al., 2020a; Pollock and Wartman, 2025; Whittall, 2020) and provide a computationally efficient means of representing the volume-dependent mobility of debris avalanches and rock avalanches.

Flow-type movement is represented using the two-parameter PCM formulation of Perla et al. (1980). The model balances gravitational acceleration against losses associated with sliding friction and velocity-dependent resistance, allowing mobility to respond to the terrain crossed by the routed material. Although originally developed for snow avalanches, PCM-type formulations have subsequently been applied to debris-flow and landslide-runout modelling (e.g. Gamma, 2000; Goetz et al., 2021; Mergili et al., 2012; Wichmann, 2017).

Within the LS-IPM, these formulations are not used to assign a deterministic movement type to an individual source. Instead, sediment production associated with each trigger and volume class is routed using both model configurations, and their contributions are subsequently weighted by the assumed relative probability of each movement mode. This allows alternative transport behaviour to be incorporated without requiring prior identification of the landslide type associated with every potential source cell. The movement-mode proportions and runout parameters adopted for the West Coast application are described in Sect. 3.

Both GPP configurations include deposition and sink filling. Because the model does not explicitly simulate entrainment and redistribution of material along an evolving landslide path, a volume-dependent smoothing of the routing surface is also applied. For each landslide-volume class, the DEM is median-filtered using a moving-window diameter related to the cube root of the geometric-mean landslide volume. This progressively suppresses topographic roughness at scales smaller than the characteristic landslide, allowing larger-volume movements to be less strongly controlled by minor terrain irregularities.

This remains a reduced-complexity treatment of landslide movement. Processes that depend strongly on momentum, internal deformation, fragmentation or dynamic interaction with topography are not explicitly resolved. In particular, the routing formulation cannot reproduce run-up or overtopping of topographic barriers in the manner of a fully dynamic runout model. These limitations must be considered when interpreting the regional results.

2.4.4 Derivation of landslide-debris flux

A complete LSD calculation consists of an ensemble of GPP simulations spanning the landslide-volume classes, triggers, return-interval ranges and movement modes represented within the LS-IPM. Each simulation therefore routes one component of the total sediment-production budget established by the LSP model.

The material-flux fields produced for the alternative movement modes are weighted by their relative probabilities $P_{(\mu)}$, where μ denotes the runout-model configuration. The ensemble is then summed and normalised by the integration interval to obtain landslide-debris flux:

$$\Phi_{L(x,y)} = \sum \frac{\Phi_{GPP(\mu)(c)(T,RI)(x,y)}}{\sigma} \times P_{(\mu)} \qquad (19)$$

where $\Phi_{GPP(\mu)(c)(T,RI)(x,y)}$ is the material flux calculated for an individual GPP simulation and σ is the same integration interval presented in Eq. (18). For mean-annual calculations, $\Phi_{L(x,y)}$ has units of m^3 m^{-2} yr^{-1}, and represents the expected volume of landslide-derived sediment passing through a unit area per year. Scenario- or event-specific source terms can be routed through the same framework to produce an event-integrated debris flux m^3 m^{-2} $event^{-1}$; derivation of these source terms is described in Sect. 2.5.

Importantly, Eq. (19) does not represent an ensemble of prescribed landslide events. Each component of the sum represents a portion of the sediment-production budget associated with a particular source-volume, trigger and movement-mode combination. The final debris-flux field therefore integrates the contributions of all feasible landslide sources affecting a location while preserving the sediment-production constraint established by the LSP model. In this way, the LSD model converts the rate-limited sediment supply into the spatially continuous hazard-intensity metric used by the LS-IPM.

2.5 Evaluation of scenario-specific landslide debris inundation hazard

The LS-IPM can be applied to both long-term mean conditions and individual triggering scenarios without changing the underlying source-to-runout framework. The distinction lies in how the landslide sediment source term is defined.

For mean-annual calculations, the LSS model partitions long-term sediment production among trigger types and return-interval bands, and the resulting source terms are propagated through the LSD model to obtain annualised debris flux. Scenario calculations instead condition sediment production on a specified set of triggering conditions. The same landslide-volume distributions, kinematic source constraints and runout formulations can then be applied, but the resulting debris flux represents the sediment response associated with that scenario rather than a long-term annual rate.

This provides a consistent basis for comparing present-day, future-climate and event-specific hazard within the same modelling framework. In all cases, the principal requirement is to define how the triggering condition modifies either the probability of landslide initiation, the amount of sediment available for mobilisation, or both.

2.5.1 Future climate scenarios

Future climate conditions can be represented within the LS-IPM by modifying the long-term balance between landslide susceptibility and sediment production. This is necessary because a sustained increase in landslide occurrence cannot be accommodated indefinitely without a corresponding change in the amount of material available for failure, or in the characteristic size distribution of the resulting landslides.

For the implementation considered here, we make two simplifying assumptions:

- earthquake-induced landslide sediment-production rates remain unchanged under the future climate scenario; and
- the characteristic volume distribution of rainfall-induced landslides remains the same as under present-day conditions.

Under these assumptions, the first step is to recalculate the mean annual landslide probability using the rainfall-induced susceptibility associated with the future climate scenario. The combined annual probability becomes:

$$P_{RCP(x,y)} = P_{RIL\_RCP(x,y)} + P_{EIL(x,y)} \qquad (20)$$

Where $P_{RIL\_RCP(x,y)}$ is the annualised rainfall-induced landslide probability under the future climate scenario and $P_{EIL(x,y)}$ retains its present-day value.

An increase in rainfall-induced susceptibility changes the relative contribution of rainfall-triggered landsliding to the annual landslide budget. If the characteristic landslide-volume distribution is held constant, this increase also requires a corresponding increase in the long-term sediment supply available to support the additional landsliding. We represent this change using a weathering-rate multiplier W, defined from the relative change in total annual landslide probability:

$$W = 1 + \frac{P_{RCP(x,y)} - P_{(x,y)}}{P_{(x,y)}} \qquad (21)$$

The adjusted landslide sediment-production rate is then:

$$\dot{E}_{L\_S\_RCP(x,y)} = \dot{E}_{L(x,y)} \times W \qquad (22)$$

The resulting source term is repartitioned among landslide triggers and volume classes using the same procedure described in Sect. 2.3 and routed through the LSD model using the formulation in Sect. 2.4.

This treatment is intentionally simple. It does not attempt to represent the individual physical processes through which climate change may alter long-term sediment supply, such as changes in weathering, vegetation, glacial retreat or soil development. Instead, it provides a means of maintaining internal consistency between an imposed increase in landslide susceptibility and the sediment-production constraint that underpins the LS-IPM. The assumptions adopted for the West Coast RCP6 application are described in Sect. 3.4.

2.5.2 Specific triggering conditions

The same framework can be used to evaluate debris inundation associated with a defined rainfall or earthquake trigger. Here it is useful to distinguish between scenario-based and event-based susceptibility fields.

Scenario-based susceptibility describes the response to a prescribed level of forcing, such as a 50-year rainfall intensity or a specified level of earthquake shaking. The assigned trigger magnitude may be spatially uniform in recurrence terms, even though the corresponding susceptibility varies across the landscape.

Event-based susceptibility instead describes the spatially variable forcing associated with a particular observed or hypothetical event. In this case, the susceptibility field is conditioned directly on the realised distribution of rainfall, shaking or another trigger.

The LS-IPM calculation is identical for both cases; only the interpretation differs. Event-based outputs represent the integrated debris response to the particular forcing field supplied to the model and can therefore be compared directly with observations from that event. Scenario-based outputs describe the conditional response where the prescribed trigger intensity is realised and should not be interpreted as the debris generated by a single spatially coherent event unless the imposed forcing itself represents such an event.

For a specified trigger scenario, the annualization applied in Eq. (17) is removed. Instead, sediment production is scaled by the susceptibility associated with the scenario relative to the mean annual probability of failure. The resulting scenario-specific sediment production is:

$$E_{L_S(x,y)} = \dot{E}_{L(x,y)} \times \frac{S_{T(x,y)}}{P_{(x,y)}} \quad (23)$$

where $S_{T(x,y)}$ is the landslide susceptibility associated with the specified triggering condition.

Because $S_{T(x,y)}$ is not an annual probability, Eq. (23) converts the long-term sediment-production rate from units of (m yr^{-1}) to a scenario-specific contribution (m $event^{-1}$). The resulting sediment is then partitioned among feasible landslide-volume classes and movement modes and routed through the LSD model in the same manner as the mean-annual source terms.

As with the annualised formulation, the scenario calculation does not identify the exact landslide sources or volumes that will occur during a particular event. Instead, it represents the expected spatial distribution of debris production conditioned on the supplied trigger field. Consequently, the resulting debris-flux maps should be interpreted as probabilistic or expected hazard fields rather than deterministic predictions of individual landslide runout paths.

3 West Coast case-study implementation

The LS-IPM framework described in Sect. 2 was applied to the approximately 25,000 km^2 West Coast region of the South Island of New Zealand at a nominal grid resolution of 25 m. The implementation combines regionally consistent rainfall- and earthquake-induced landslide susceptibility models, long-term estimates of sediment production, empirically constrained landslide-volume distributions, and reduced-complexity runout modelling. Detailed documentation of the underlying regional datasets and their derivation is provided by Leith et al. (2025b); here we summarise the inputs and parameter choices required to reproduce the application presented in this study.

3.1 Landslide source-susceptibility inputs

Rainfall- and earthquake-induced landslide susceptibility were represented using statistical models previously developed for New Zealand (Massey et al., 2021; Rosser et al., 2021). Rainfall-induced landslide susceptibility was evaluated for 24-hour rainfall associated with 50-, 100- and 250-year annual recurrence intervals (ARIs), using rainfall estimates from the NIWA HIRDS V4 model (NIWA Taihoro Nukurangi, 2022). Although landsliding can respond to rainfall accumulated over a range of durations, 24-hour rainfall was adopted as a consistent regional predictor for this application. Earthquake-induced landslide susceptibility was evaluated for 100-, 250-, 500- and 1000-year ARI peak ground accelerations derived from the 2022 New Zealand National Seismic Hazard Model (Gerstenberger et al., 2022). These rainfall- and earthquake-induced susceptibility fields were annualised and combined using Eqs. (1) - (3). The source-area terms required by Eqs. (1) and (2) were derived from regional landslide inventories as described in Leith et al. (2025b).

For the scenario-based Alpine Fault calculation, the regional earthquake susceptibility model was instead forced using the spatially variable PGA field from the AlpineF2K M_W 8 rupture scenario of Bradley et al. (2017).

3.2 Landslide sediment-production inputs

3.2.1 Long-term sediment supply

The spatial pattern of long-term erosion was estimated from nationally consistent suspended-sediment-yield data (Hicks et al., 2011) together with mapped geological densities (Tenzer et al., 2011). Because suspended load represents only part of the total sediment export, suspended sediment yield was multiplied by 1.5 before conversion to an erosion rate. This factor was selected by comparison with independent estimates of uplift and catchment-scale denudation in the Southern Alps (Adams, 1980; Hovius et al., 1997; Roda-Boluda et al., 2023), see Leith et al. (2025b) for further details.

For the calculation in Eq. (4), we assume that primary erosion from terrain identified as kinematically capable of landsliding is attributable to landslide processes, i.e. $\omega_L = 1$. A bulking factor of η_L = 1.3 was applied to convert in-situ erosion volumes to landslide debris volumes, and a representative debris density of 2000 kg m^{-3} was adopted. The assumption $\omega_L = 1$ provides a conservative upper-bound treatment of landslide-derived sediment production and is most likely to overestimate production where other erosional processes make a substantial contribution, particularly in glacierised terrain.

3.2.2 Kinematic source parameters

The kinematic source model described in Sect. 2.3.2 was applied using θ_{XST} = 20° to define the limiting basal-failure geometry and θ_{NAT} = 20° for the supplementary shallow-failure criterion. The adopted basal angle lies within the approximately 8° – 27° range of back-calculated strengths reported for large landslides in comparable soil and rock materials by Alberti et al. (2022). A representative cohesive strength of 50 kPa was used in Eq. (6). This value is near the upper end of the back-calculated range presented by Alberti et al. (2022), but remains substantially below values reported for fractured New Zealand greywacke rock masses (Read et al., 1999). It was therefore adopted as a regional-scale compromise intended to represent a mixture of soil, weathered bedrock and fractured rock rather than any particular local material. These values were applied consistently across the study area. Local variation in material strength was not represented.

3.2.3 Landslide-volume distributions

Trigger-specific landslide-volume distributions were derived from regional inventories for which event coverage was considered sufficiently complete. These comprised 6359 earthquake-induced and 7269 rainfall-induced landslide polygons (see Leith et al. (2025b) for a list of data sources). Source regions were separated from mapped runout areas, and source volumes were estimated from the 8 m national DEM (LINZ, 2012) using the kinematic procedure described in Sect. 2.3.2. Details of the statistical analysis of landslide source geometries are provided in Leith et al. (2025b). In summary, both trigger populations were approximated by log-normal volume distributions, consistent with the general form identified by Brunetti et al. (2009). The earthquake-induced population has a geometric-mean $\log_{10}$ source volume of 4.55 with a standard deviation of 0.60, while the rainfall-induced population has a geometric mean of 3.92 with a standard deviation of 0.68, with volumes expressed in $\log_{10}$ m^3. These distributions provide the trigger-dependent volume weights used in Eqs. (13) – (17); they do not determine the total long-term sediment supply.

3.3 Landslide sediment-distribution inputs

The LSD model was run on a 25 m DEM using the GPP framework of Wichmann (2017). Mean-annual simulations used an integration interval of $\sigma=10^4$ years in Eq. (18), approximately corresponding to the post-glacial interval over which the present landscape has developed. Testing integration intervals between 0.1 and 10 kyr changed mean annual debris flux in a representative area by less than 1%, although the proportion of terrain receiving some debris flux increased by 2.7% (Leith et al., 2025b). A complete mean-annual calculation comprised 112 GPP simulations representing the required combinations of trigger type, return interval, source-volume class and movement mode. Outputs were combined using Eq. (19).

3.3.1 Avalanche-type movement

Avalanche-type transport was modelled with the GPP fahrböschung formulation (Heim, 1932). Mobility for each landslide-volume class was assigned from dry open-slope debris-avalanche and rock-avalanche volume–fahrböschung relationships compiled from New Zealand and international data (Brideau et al., 2021). The 50th-percentile fahrböschung corresponding to the geometric-mean volume of each class was used, and the same relationships were applied to rainfall- and earthquake-induced sources.

3.3.2 Flow-type movement

Flow-type transport was represented using the PCM formulation of Perla et al. (1980) within GPP. In the absence of a regional dataset suitable for direct optimisation of PCM parameters, we adopted parameter values based on debris-flow modelling in Switzerland (Gamma, 2000; Wichmann, 2017), with drag varied as a function of contributing catchment area to increase mobility in channelised terrain. Model behaviour was checked qualitatively against mapped debris-flow extents on West Coast fans; further detail is provided by Leith et al. (2025b). Both movement configurations employed GPP deposition and sink-filling.

3.3.3 Movement-mode weighting

No regional inventory was available that consistently distinguished avalanche- and flow-type runout for the West Coast. Rainfall-induced movement-mode weights were therefore estimated from landslides mapped following Cyclone Gabrielle (Leith et al., 2025a), for which approximately 66% of mapped movements were classified as avalanche-type and 33% as flow-type. These proportions were transferred to the West Coast rainfall-induced calculation. Flow-type behaviour was assumed to be less common for earthquake-induced landsliding. We therefore assigned earthquake-induced sediment production using weights of 83% avalanche-type and 17% flow-type. These weights enter the ensemble summation through $P_{(\mu)}$ in Eq. (19) and should be regarded as regional model assumptions rather than locally calibrated probabilities.

3.4 Future-climate and earthquake scenarios

The RCP6 2081–2100 calculation was implemented using the same model geometry, landslide-volume distributions and runout parameters as the present-day calculation. Rainfall inputs to the LSS model were adjusted in accordance with the HIRDS V4 future-climate projections, producing the future rainfall-induced probability $P_{RIL\_RCP(x,y)}$ used in Eq. (20). The corresponding change in long-term sediment supply was then calculated using Eqs. (21) and (22). Earthquake-induced source probability and the rainfall- and earthquake-induced landslide-volume distributions were held fixed. Further details of the regional climate adjustment are given in Leith et al. (2025b).

The Alpine Fault calculation used the same kinematic source, landslide-volume and runout parameterisation as the mean-annual earthquake model, but replaced the ARI-based shaking fields with the AlpineF2K M_W 8 PGA field of Bradley et al. (2017). Scenario sediment production was calculated using Eq. (23), and the resulting source fields were routed through the same LSD configurations used for the annualised model.

4 Results

4.1 Regional controls on landslide source activity and sediment production

The mean annual LSS outputs show a strong regional contrast in both the magnitude and dominant trigger of landslide activity (Figure 2). The highest source probabilities occur along the Southern Alps between approximately Fox Glacier and Kokiraki, where steep terrain coincides with high rainfall-induced susceptibility. Rainfall-induced landsliding generally dominates along this range front, whereas earthquake-induced source probabilities make a greater relative contribution in the northern part of the study area. Around Kokiraki, for example, the spatially averaged rainfall-induced source probability is approximately 0.30 kyr^{-1}, compared with approximately 0.10 kyr^{-1} for earthquake-induced landsliding. Northeast of Greymouth, the relative ordering is reversed, although absolute source probabilities are lower (Figure 2).

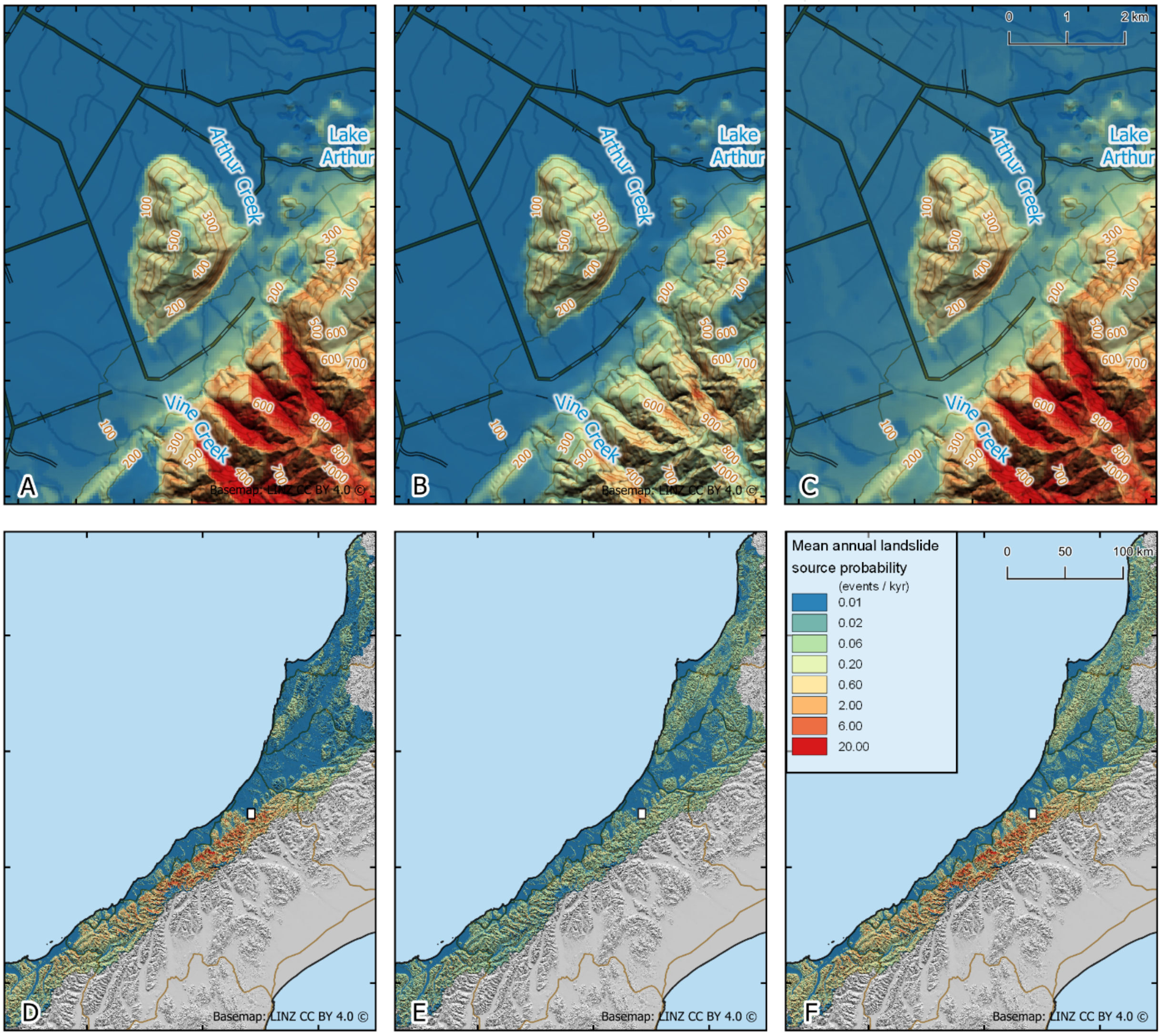

Figure 2: Selection of landslide source-susceptibility model outputs. (a, d) Mean annual rainfall-induced landslide probability. (b, e) Mean annual earthquake-induced landslide probability. (c, f) Total mean annual source probability. Legend categories are consistent across all maps. The location of the Kokiraki maps (a–c) are indicated by a white box on the regional overview maps. Reproduced from Leith et al. (2025b).

In contrast to these trigger-dependent patterns, the total long-term sediment supply is constrained independently by the regional erosion model. Present-day landslide sediment-production rates show a pronounced regional gradient (Figure 3). Rates are commonly around 6 mm yr^{-1} along the main range front and locally approach 30 mm yr^{-1} in the Aoraki/Mount Cook region, while values in the northern part of the study area are closer to 0.25 mm yr^{-1}. Catchment-scale averages are consistent with independent estimates of uplift and denudation in the Southern Alps (Adams, 1980; Hovius et al., 1997; Roda-Boluda et al., 2023), providing an independent constraint on the order of magnitude of sediment supplied to the runout model. See Leith et al. (2025b) for further details on their correlation.

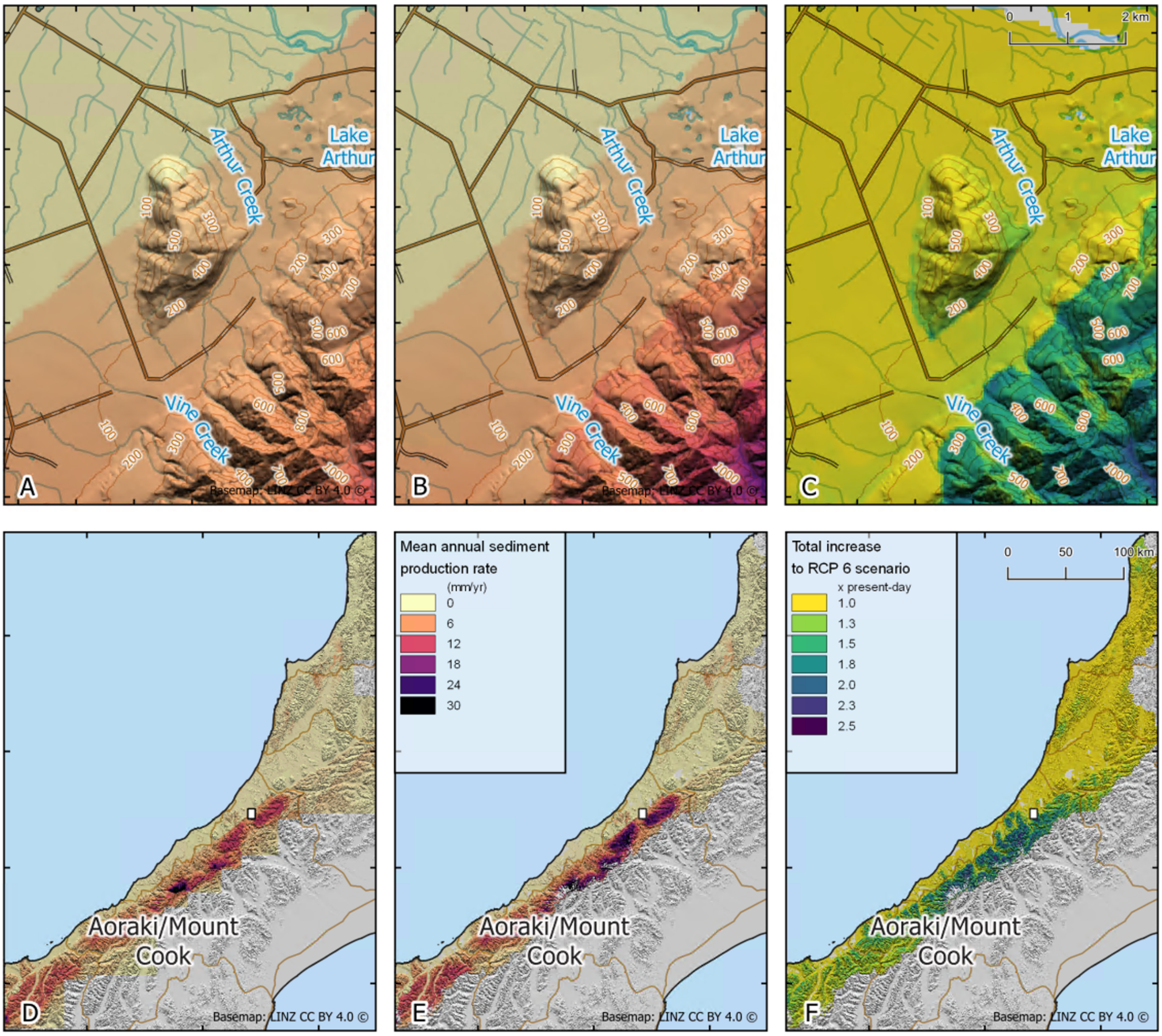

Figure 3: Selection of landslide sediment-production model outputs. (a, d) Mean annual sediment production. (b, e) Mean annual sediment production for the RCP6 2081–2100 climate scenario. (c, f) Change in total mean annual sediment production. Legend categories are consistent across maps (a), (b), (d) and (e) and maps (c) and (f). The location of the Kokiraki maps are indicated by a white box on the regional overview maps. Reproduced from Leith et al. (2025b).

4.2 Mean annual landslide-debris flux

Routing the source terms through the LSD model converts these spatial variations in sediment supply, source size and trigger probability into a markedly different pattern of debris-inundation hazard (Figure 4). High mean annual debris flux is not confined to locations with high source probabilities. Instead, elevated values extend downslope from productive source terrain and become locally concentrated where topography focuses transport into gullies, channels and valley axes. Debris flux is therefore controlled jointly by the amount of sediment generated upslope and the efficiency with which the landscape connects those sources to a given location.

This distinction is evident around Kokiraki, where high debris flux occurs both on steep source slopes and on lower-gradient terrain receiving material from multiple contributing hillslopes (Figure 4). The maximum modelled reach is generally associated with the largest landslide-volume classes permitted by the kinematic source model, whereas the magnitude of flux within the inundated area reflects the accumulated contribution from the complete range of feasible sources, triggers and movement modes. Thus, the debris-flux field contains information that is absent from source susceptibility alone: two locations with similar local susceptibility can experience substantially different inundation hazard where their upslope sediment supply or topographic connectivity differs. The regional model indicates that a large majority of the study area is intersected by at least some modelled landslide-derived debris flux.

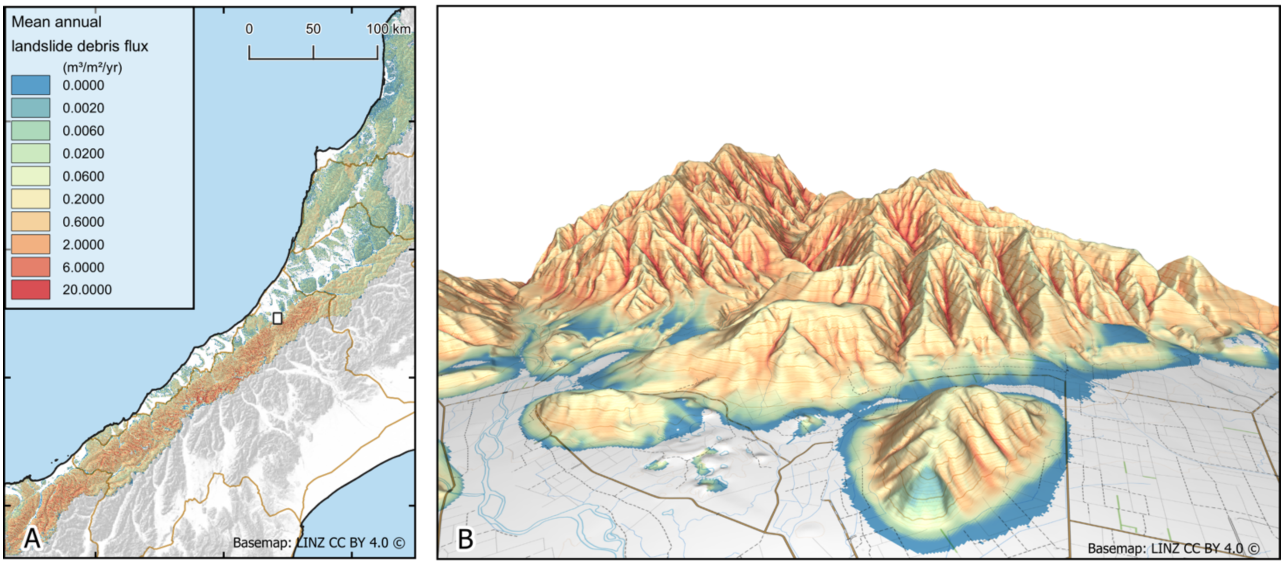

Figure 4: Present-day mean annual landslide-debris flux in the vicinity of Kokiraki (vertical exaggeration 1.25×). Reproduced from Leith et al. (2025b).

4.3 Response to the RCP6 2081–2100 climate scenario

The RCP6 calculation increases rainfall-induced source probability over much of the region (Figure 5), with the strongest proportional changes broadly following areas already susceptible to rainfall-induced failure. Under the assumptions in Sect. 2.5.1, this increased source activity is balanced by an increase in the long-term supply of landslide sediment. The resulting regional mean increase in landslide sediment production is approximately 50%. This is comparable in scale, although not directly equivalent, to the 31% increase in regional sediment yield estimated for the same climate scenario by Neverman et al. (2023).

The response of debris flux is spatially non-uniform (Figure 6). The outer limit of modelled inundation changes comparatively little because the kinematic constraints on maximum source size and the mobility assigned to individual volume classes are unchanged. Changes are instead expressed mainly as increased flux within the existing hazard footprint. On many fans and moderate-gradient hillslopes, the increase is broadly comparable with the approximately twofold increase in local rainfall-driven sediment supply. In parts of the high-relief alpine belt, however, debris flux increases by substantially more than the local change in sediment production and can locally approach an order-of-magnitude increase. This amplification occurs where additional debris from multiple upslope sources converges along common transport pathways.

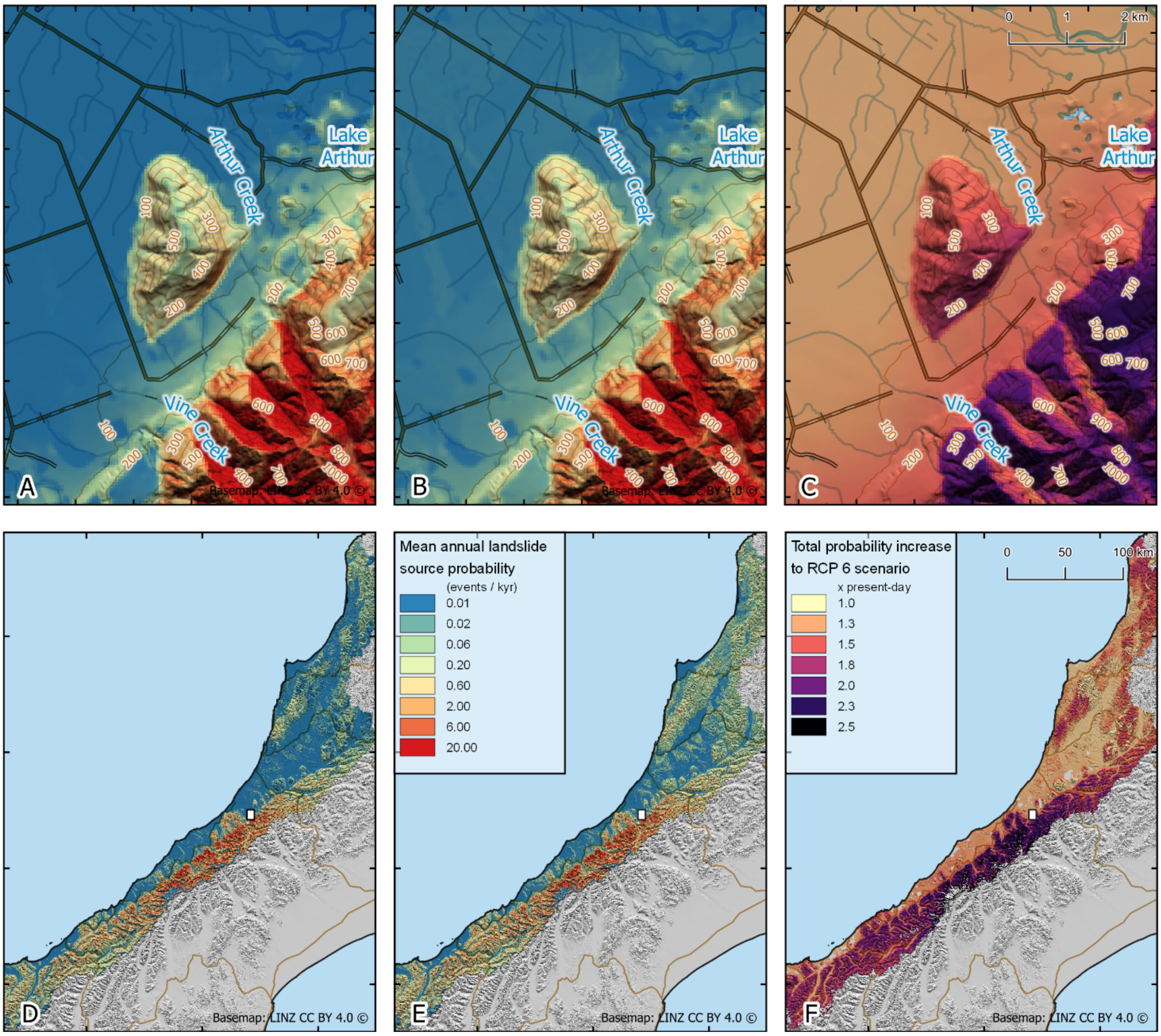

Figure 5: Selection of landslide source-susceptibility model outputs for the RCP6 2081– 2100 climate scenario. (a, d) Mean annual probability of rainfall-induced landslide occurrence. (b, e) Total mean annual probability of landslide occurrence, (c, f) Change in total mean annual source probability from present-day probability. Legend categories are consistent across maps (a), (b), (d) and (e) and maps (c) and (f). The location of the Kokiraki maps are indicated by a white box on the regional overview maps. Reproduced from Leith et al. (2025b).

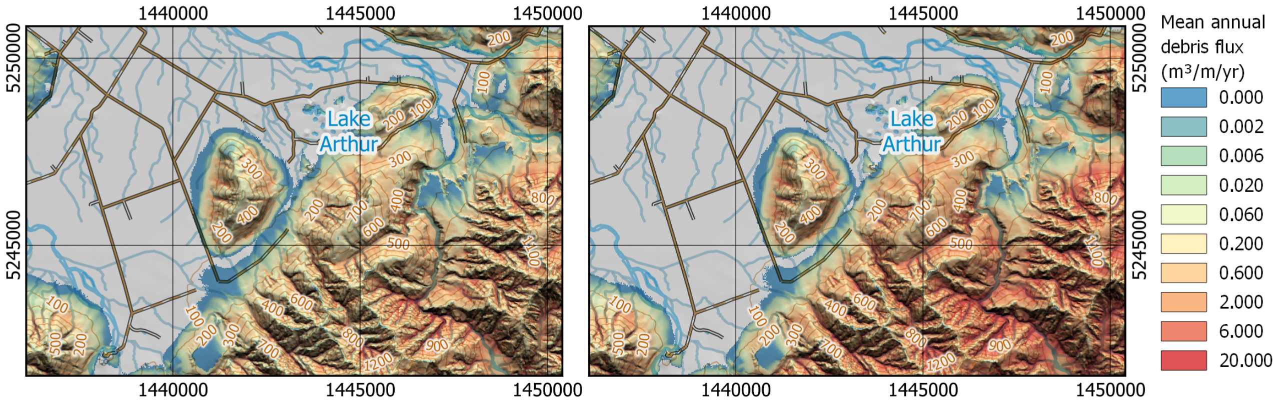

Figure 6: Left: Present-day mean annual landslide debris flux. Right: RCP6 2081–2100 mean annual debris flux, assuming rainfall-triggered landslide sediment production rates increase in concert with predicted increases in susceptibility. Reproduced from Leith et al. (2025b).

4.4 Alpine Fault earthquake scenario

The Alpine Fault scenario provides a complementary test of the event-integrated formulation because the source field is conditioned on the spatially variable PGA predicted by the AlpineF2K rupture model (Bradley et al., 2017). Across the modelled region, scenario-integrated debris flux for inundated cells is approximately log-normally distributed (Figure 7). The geometric means of the movement-mode distributions are approximately 80–160 $m^3\,m^{-2}\,event^{-1}$, with the flow-type configuration producing a somewhat larger upper tail than the avalanche-type configuration. More than half of the inundated locations in the combined scenario exceed approximately 10^2 $m^3\,m^{-2}\,event^{-1}$. The predicted distributions are also similar in central tendency to debris-flux distributions reconstructed from mapped landslides (Leith et al., 2025b) associated with the 1929 M_W 7.3 Murchison and 1968 M_W 7.1 Inangahua earthquakes (Hancox et al., 2014, 2016). Their lower tails differ more strongly, with the historical-event datasets extending toward lower fluxes. The comparison is not fully independent because the same general GPP routing approach is used to estimate flux for the mapped landslides. However, the LSS and LSP inputs used to generate the Alpine Fault scenario do not depend on the Murchison or Inangahua inventories. Agreement in the characteristic flux therefore provides a useful check on the magnitude of debris emerging from the complete source-to-inundation workflow, rather than an independent validation of the runout algorithm itself.

Movement mode has a stronger influence on the high-intensity tail than on the first-order extent of inundation. In the AF8 simulations, flow-type routing affects approximately 80% of the model domain at the lowest plotted flux thresholds compared with approximately 72% for avalanche-type routing, and retains a greater proportion of area at progressively higher thresholds (Figure 7). The combined model lies between these end members. This indicates that movement-mode assumptions primarily modify the distribution of debris intensity within connected runout pathways, whereas the broad spatial footprint remains strongly constrained by source availability and topographic connectivity.

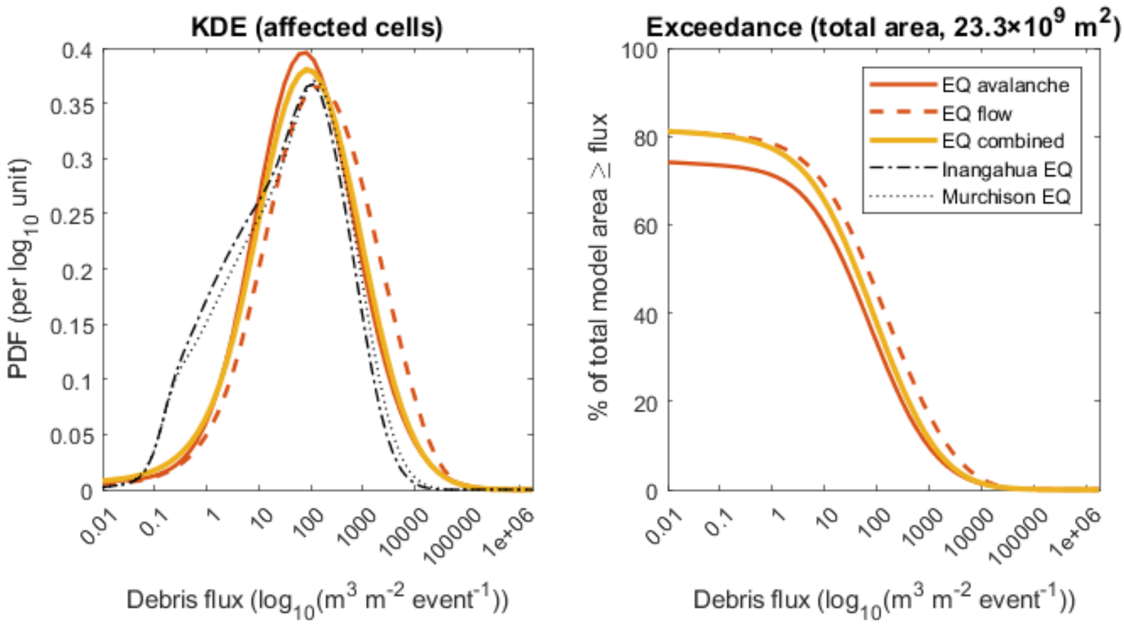

Figure 7: Left: Kernel density estimate for predicted landslide debris fluxes resulting from the AF 8 PGA scenario across the study region, as well as modelled debris fluxes associated with mapped landslides triggered by the Murchison, and Inangahua earthquakes. Right: Percentage of study region associated with given fluxes resulting from AF 8 PGAs.

5 Discussion

5.1 From landslide susceptibility to debris-inundation hazard

The West Coast application illustrates an important distinction between landslide source susceptibility and debris-inundation hazard. Source probability determines where sediment is preferentially mobilised and how the available sediment budget is divided among triggers and landslide sizes. It does not, however, independently determine the total long-term sediment supply. Within the LS-IPM formulation, that quantity is constrained by erosion rates through Eq. (4), while the LSS model provides the relative allocation required by Eq. (17). This means that a region with high susceptibility does not automatically generate an arbitrarily high long-term landslide frequency: increasing the contribution from one trigger or landslide-size class must be accommodated within the available sediment budget.

The West Coast results demonstrate why this distinction matters spatially. Rainfall-induced source activity dominates much of the main range front, whereas earthquake-induced landsliding makes a larger relative contribution farther north. Because the earthquake-induced source-volume distribution is shifted toward larger failures, changing the relative importance of the two triggers also changes the proportion of sediment assigned to more mobile landslides. Hazard at a distal location therefore reflects not simply whether upslope terrain is susceptible to failure, but the combination of source probability, characteristic landslide size, sediment production and connectivity.

This is the principal difference between the LS-IPM and approaches in which regional hazard is assembled from a prescribed population of discrete events. The frequency-magnitude balance emerges here from the sediment-production constraint rather than being specified through the number of simulated landslides. The West Coast implementation consequently uses mapped landslides to describe the relative distribution of source sizes and trigger response, while independent geomorphic information constrains the total volume of debris that can be generated through time.

5.2 Debris flux as a regional hazard-intensity metric

The modelled debris-flux patterns also clarify what is—and is not—represented by the LS-IPM hazard metric. Flux integrates the effects of sediment magnitude and occurrence frequency and is therefore well suited to comparing the relative intensity of landslide-derived sediment transfer across a large landscape. It also allows contributions from many potential source areas to accumulate naturally within shared transport pathways, which is particularly important in convergent topography. However, mean annual debris flux does not uniquely identify the frequency or magnitude of the individual events responsible for that flux. A location receiving the same long-term flux could theoretically experience many small failures or a much smaller number of large events. Separation of these quantities requires the additional probability formulation developed in Part 2 (Leith and Wichmann, 2026). The principal role of the present model is therefore to establish a spatially continuous, mass-constrained hazard-intensity field from which those subsequent frequency and risk metrics can be derived.

The concentration of modelled flux within valleys and on depositional landforms is particularly relevant in this respect. These locations may have little or no local source susceptibility, yet can receive material generated across a comparatively large contributing area. This behaviour is one reason that source-susceptibility mapping alone is insufficient for regional debris-inundation assessment.

5.3 What the climate scenario demonstrates about the process-based formulation

The RCP6 experiment highlights both an advantage and a limitation of the process-based approach. Increasing rainfall susceptibility alone would increase the expected number of landslides without addressing the material required to sustain them. If the characteristic landslide-volume distribution remains unchanged, an internally consistent long-term calculation must therefore either increase sediment production or invoke some compensating reduction in landslide volume.

The implementation adopted here explores the first end member by increasing sediment production in proportion to the change in annual landslide probability. The resulting approximately 50% regional increase should therefore not be interpreted as a direct prediction of future erosion. Rather, it quantifies the consequences of the explicit assumption that increased rainfall-triggered activity is sustained by a corresponding increase in sediment availability.

This distinction is important because climate-driven hillslope response may involve changes in weathering, deglaciation, vegetation, soil production and antecedent disturbance, all acting over different timescales. A rapidly changing climate may also drive temporary disequilibrium between the production of failure-prone material and its removal by landsliding. The strength of the LS-IPM formulation is that such processes can, where independently constrained, be introduced through the sediment-production term rather than being implicitly absorbed into a statistical extrapolation of historical landslide frequency. The present RCP6 calculation demonstrates that capability rather than resolving the physical evolution of West Coast sediment supply.

The spatial response further shows that changes in source production need not translate linearly into changes in downstream hazard. Where transport from multiple slopes converges, an approximately twofold increase in source material can produce substantially larger changes in local debris flux. Conversely, the maximum inundation footprint changes little where maximum feasible source size and mobility remain fixed. This separation between changes in hazard intensity and changes in hazard extent is a useful property of the process-based framework.

5.4 Event-based application and model evaluation

The Alpine Fault scenario provides a stronger test of the event-based use of LS-IPM than the spatially uniform ARI scenarios because it applies a physically coherent, spatially variable shaking field derived from Bradley et al. (2017). The similarity between the characteristic AF8 debris flux and the flux reconstructed from the Murchison and Inangahua inventories is encouraging, particularly because the source susceptibility and sediment-production components are independently derived from those historical inventories.

The comparison should nevertheless be interpreted cautiously. It cannot be regarded as a fully independent validation of runout performance because the mapped-event fluxes are also evaluated using GPP. What it does test more independently is whether the combination of source susceptibility, feasible source volumes and event-scale sediment production generates a regional debris budget of a plausible magnitude. The agreement in the centres of the distributions, together with differences in their tails that are consistent with differences in relief and opportunities for channelisation, suggests that the framework captures at least the first-order event-scale characteristics represented by these historical earthquakes.

A stronger future evaluation would compare LS-IPM event outputs directly against independent observations of landslide source volume, transported sediment volume and spatial inundation following a well-mapped event. Such data would allow the LSS, LSP and LSD components to be tested separately rather than judging the combined model from the final flux distribution alone.

5.5 Limitations and transferability

The regional character of the LS-IPM necessarily requires simplification. In the West Coast implementation, uncertainties remain in the regional erosion field, assumed landslide-volume distributions, kinematic source parameters, movement-mode proportions and GPP mobility parameters. DEM resolution and accuracy additionally control the representation of small source landforms and transport pathways. These uncertainties are evaluated in detail in Part 2 (Leith and Wichmann, 2026), and the present results should therefore be interpreted as regional hazard estimates rather than predictions of individual landslide behaviour.

These same simplifications, however, make the framework transferable. Application in another region does not require the West Coast parameterisation to be retained. It requires independent constraints on the long-term sediment budget, appropriate landslide susceptibility and volume distributions, a representation of feasible source size, and mobility parameters suited to the dominant movement processes. Where these inputs can be estimated, the same mass-balance and routing formulation can be applied without first defining a representative catalogue of hypothetical regional landslide events.

The LS-IPM is consequently complementary to, rather than a replacement for, higher-complexity runout models. Dynamic models remain preferable where the objective is to reconstruct a particular landslide or estimate velocity, flow depth and impact forces at a site. The advantage of the LS-IPM lies instead in providing a computationally tractable means of propagating physically constrained landslide sediment production through an entire landscape and expressing the result using a consistent regional hazard metric.

6 Conclusions

This study presents the Landslide Source-to-Inundation Process Model (LS-IPM), a regional-scale framework for estimating landslide debris inundation hazard by treating landsliding as a spatially distributed, rate-limited sediment-production and transport process. Rather than defining hazard from a prescribed set of discrete landslide scenarios, the LS-IPM couples landslide source susceptibility, landslide sediment production, and mass-conservative downslope debris routing to generate spatially continuous fields of landslide-derived debris flux. In this formulation, hazard intensity is expressed as the volume of landslide debris expected to pass through or accumulate at a location, either as a mean annual quantity or as an event-integrated scenario output.

The central methodological advance of the LS-IPM is that landslide magnitude and frequency are constrained through a geomorphologically informed sediment-production rate, rather than specified independently through scenario design. Landslide debris production is distributed across kinematically feasible source areas and volume classes, then routed downslope using a reduced-complexity gravitational process model. This allows the cumulative contribution of all feasible landslide sources to be evaluated efficiently, including the combined effects of many small, frequent failures and larger, less frequent landslides. As a result, landslide debris inundation hazard can be mapped continuously across large regions without explicitly enumerating every possible landslide source, volume, and runout path.

Application of the LS-IPM to the ~25,000 km^2 West Coast region of New Zealand demonstrates that landslide debris inundation hazard is controlled by the interaction between source productivity, topographic relief, and downslope connectivity. Modelled debris flux is highest on steep slopes, near the base of high-relief landforms, and along convergent topography such as valley axes, where debris is concentrated by runout processes. At local scales, modelled flux patterns extend to within one 25 m grid cell of mapped debris-fan margins, with higher fluxes concentrated near fan apices and along active or relict debris-flow channels. These patterns are consistent with geomorphological expectations and indicate that the LS-IPM captures first-order controls on regional debris redistribution.

The West Coast application also highlights the scale of landslide debris inundation hazard in steep, tectonically active landscapes. Approximately 80 % of the study region is affected by some degree of modelled landslide debris inundation hazard. Future climate scenarios increase mean annual debris flux by approximately 50 %, indicating that changes in landslide triggering frequency and sediment production may substantially alter regional debris-hazard patterns. Under an Alpine Fault Mw 8.0 earthquake scenario, more than half of affected locations are expected to experience event-integrated debris fluxes exceeding 10^2 m^3 m^{-2} $event^{-1}$, emphasising the potential for co-seismic landsliding to generate widespread, high-intensity debris inundation across the central Southern Alps.

By expressing hazard as debris flux, the LS-IPM provides a direct link between geomorphic process understanding and hazard metrics suitable for subsequent risk analysis. The approach bridges a gap between landscape-evolution models, which are well suited to representing long-term sediment production and redistribution but generally do not produce risk-ready inundation metrics, and applied landslide risk models, which can estimate consequences but typically rely on scenario-based runout footprints or incomplete landslide inventories. The LS-IPM therefore provides a process-based means of incorporating long-term erosion constraints, landslide inventory statistics, kinematic source feasibility, and downslope debris routing within a single regional hazard framework.

The outputs presented here are deliberately limited to hazard-intensity metrics expressed as landslide debris flux. Although debris flux integrates information about both landslide magnitude and frequency, it does not itself constitute a complete measure of risk, which requires explicit treatment of inundation probability, exposure, and vulnerability. These elements are addressed in Part 2 of this study (Leith and Wichmann, 2026), where LS-IPM outputs are translated into probabilities of inundation and building-scale risk metrics. This separation clarifies the role of the LS-IPM as a hazard-generation model and provides a transparent basis for evaluating model assumptions before exposure and vulnerability are introduced.

Overall, the LS-IPM represents a step forward for regional landslide debris inundation hazard assessment because it enables runout-informed hazard to be evaluated across very large areas at practical spatial resolution while avoiding the need to prescribe a finite set of landslide scenarios. An additional advantage of the process-based formulation is that it provides a pathway for incorporating physical drivers of future change that are difficult to represent in statistical models calibrated only to historical landslide inventories. These may include changes in sediment-production rates arising from accelerated weathering, altered soil-erosion rates, wildfire-related vegetation loss, canopy damage, root-strength degradation, or other changes in hillslope material supply and stability. Where these effects can be independently constrained, they can be introduced through adjustments to susceptibility, sediment-production, or routing parameters, rather than inferred indirectly from past landslide frequencies. For regions such as the West Coast, where landslide inventories are incomplete, triggering events are infrequent, and geomorphic rates provide important constraints on future behaviour, this flux-based formulation provides a scalable and physically grounded foundation for regional hazard and risk analysis under both present-day and changing environmental conditions.

7 DATA AND CODE AVAILABILITY

The method contains the information necessary to reproduce the results of this study. All computations for the hazard analysis were undertaken in MATLAB 2023a, using TopoToolbox 2 and SAGA 9.2. The required scripts, and input data are available at https://doi.org/10.17605/OSF.IO/WV3NJ. All additional data, software, and functions are publicly available in the references.

8 Author Contribution

KL conceptualised the study, developed the methodology, undertook the investigation, performed the formal analysis, prepared the visualisations, wrote the original draft, and led review and editing of the manuscript. CM undertook modelling, contributed to the methodology, and wrote parts of the manuscript. BL undertook numerical analyses and contributed to the interpretation of model outputs. VW developed code, contributed to the modelling framework, and wrote parts of the manuscript. All authors reviewed and approved the final manuscript.

9 Competing Interest

The authors declare that they have no conflict of interest.

10 Acknowledgements

The authors would like to acknowledge reviews by Dr Feiko van Zadelhoff and Dr Andrew Neverman (Manaaki Whenua – Landcare Research, now part of the Bioeconomy Science Institute), Sally Dellow (Earth Sciences New Zealand) and Dr Sam McColl (Earth Sciences New Zealand), as well as input provided by Edith Bretherton, and Scott Kelly (Earth Sciences New Zealand).

11 References

Aaron, J.: ORIN-3D – A new model for efficient simulation of landslide motion on a GPU using CUDA, Comput. Geotech., 153, 105078, 2023.

Adams, J.: Contemporary Uplift and Erosion of the Southern Alps, New Zealand, GSA Bulletin, 91, 1–114, 1980.

Barnhart, K. R., Jones, R. P., George, D. L., McArdell, B. W., Rengers, F. K., Staley, D. M., and Kean, J. W.: Multi-model comparison of computed debris flow runout for the 9 January 2018 Montecito, California post-wildfire event, J. Geophys. Res. Earth Surf., 126, e2021JF006245, 2021.

Barnhart, K. R., Kean, J. W., Lindsay, D. N., and Bilderback, E. L.: Multi-site evaluation of a Postfire debris-flow runout forecast method, Earths Future, 14, e2025EF007004, 2026.

Bera, S., Melo, R., and Guru, B.: Assessment of exposed elements in a changing built environment by using an integrated model of debris flow initiation and runout (Kalimpong region, Himalaya), Bull. Eng. Geol. Environ., 80, 7131–7152, 2021.

Blöthe, J. H., Korup, O., and Schwanghart, W.: Large landslides lie low: Excess topography in the Himalaya-Karakoram ranges, Geology, 43, 523–526, 2015.

Bradley, B. A., Bae, S. E., Polak, V., Lee, R. L., Thomson, E. M., and Tarbali, K.: Ground motion simulations of great earthquakes on the Alpine Fault: effect of hypocentre location and comparison with empirical modelling, N. Z. J. Geol. Geophys., 60, 188–198, 2017.

Brideau, M.-A., de Vilder, S., Massey, C., Mitchell, A., McDougall, S., and Aaron, J.: V1.0 Empirical Landslide Runout Relationships, compiled from international examples, for various landslide types, https://doi.org/10.17603/ds2-9qbx-n796, 2021.

Brunetti, M. T., Guzzetti, F., and Rossi, M.: Probability distributions of landslide volumes, Nonlinear Process. Geophys., 16, 179–188, 2009.

Burbank, D. W., Leland, J., Fielding, E., Anderson, R. S., Brozovic, N., Reid, M. R., and Duncan, C.: Bedrock incision, rock uplift and threshold hillslopes in the northwestern Himalayas, Nature, 379, 505–510, 1996.

Campforts, B., Schwanghart, W., and Govers, G.: Accurate simulation of transient landscape evolution by eliminating numerical diffusion: the TTLEM 1.0 model, Earth Surf. Dyn., 5, 47–66, 2017.

Campforts, B., Shobe, C. M., Steer, P., Vanmaercke, M., Lague, D., and Braun, J.: HyLands 1.0: a hybrid landscape evolution model to simulate the impact of landslides and landslide-derived sediment on landscape evolution, Geosci. Model Dev., 13, 3863–3886, 2020.

Clerici, A. and Perego, S.: Simulation of the Parma River blockage by the Corniglio landslide (Northern Italy), Geomorphology (Amst.), 33, 1–23, 2000.

Corominas, J.: The angle of reach as a mobility index for small and large landslides, Can. Geotech. J., 33, 260–271, 1996.

D'Ambrosio, D., Di Gregorio, S., Iovine, G., Lupiano, V., Rongo, R., and Spataro, W.: First simulations of the Sarno debris flows through Cellular Automata modelling, Geomorphology (Amst.), 54, 91–117, 2003.

Dymond, J. R., Betts, H. D., and Schierlitz, C. S.: An erosion model for evaluating regional land-use scenarios, Environmental Modelling & Software, 25, 289–298, 2010.

Eppes, M. C., Magi, B., Scheff, J., Warren, K., Ching, S., and Feng, T.: Warmer, wetter climates accelerate mechanical weathering in field data, independent of stress-loading, Geophys. Res. Lett., 47, https://doi.org/10.1029/2020gl089062, 2020.

Eppes, M.-C. and Keanini, R.: Mechanical weathering and rock erosion by climate-dependent subcritical cracking: WEATHERING BY SUBCRITICAL CRACKING, Rev. Geophys., 55, 470–508, 2017.

Frank, F., McArdell, B. W., Huggel, C., and Vieli, A.: The importance of entrainment and bulking on debris flow runout modeling: examples from the Swiss Alps, Nat. Hazards Earth Syst. Sci., 15, 2569–2583, 2015.

Gamma, P.: dfwalk-Ein Murgang-Simulationsprogramm zur Gefahrenzonierung, G66, 2000.

Gerstenberger, M. C., Van Dissen, R. J., Rollins, C., DiCaprio, C., Chamberlain, C., Christophersen, A., Coffey, G. L., Ellis, S. M., Iturrieta, P., and Johnson, K. M.: The Seismicity Rate Model for the 2022 New Zealand National Seismic Hazard Model, GNS Science, Lower Hutt (NZ), 156 pp., https://doi.org/10.21420/2EXG-NP48, 2022.

Goetz, J., Kohrs, R., Parra Hormazábal, E., Bustos Morales, M., Araneda Riquelme, M. B., Henríquez, C., and Brenning, A.: Optimizing and validating the Gravitational Process Path model for regional debris-flow runout modelling, Nat. Hazards Earth Syst. Sci., 21, 2543–2562, 2021.

Gorr, A. N., McGuire, L. A., Youberg, A. M., and Rengers, F. K.: A progressive flow-routing model for rapid assessment of debris-flow inundation, Landslides, 19, 2055–2073, 2022.

Guthrie, R. and Befus, A.: DebrisFlow Predictor: an agent-based runout program for shallow landslides, Nat. Hazards Earth Syst. Sci., 21, 1029–1049, 2021.

Guzzetti, F., Ardizzone, F., Cardinali, M., Rossi, M., and Valigi, D.: Landslide volumes and landslide mobilization rates in Umbria, central Italy, Earth Planet. Sci. Lett., 279, 222–229, 2009.

Han, Z., Chen, G., Li, Y., Tang, C., Xu, L., He, Y., Huang, X., and Wang, W.: Numerical simulation of debris-flow behavior incorporating a dynamic method for estimating the entrainment, Eng. Geol., 190, 52–64, 2015.

Han, Z., Li, Y., Huang, J., Chen, G., Xu, L., Tang, C., Zhang, H., and Shang, Y.: Numerical simulation for run-out extent of debris flows using an improved cellular automaton model, Bull. Eng. Geol. Environ., 76, 961–974, 2017.

Han, Z., Ma, Y., Li, Y., Zhang, H., Chen, N., Hu, G., and Chen, G.: Hydrodynamic and topography based cellular automaton model for simulating debris flow run-out extent and entrainment behavior, Water Res., 193, 116872, 2021.

Hancox, G. T., Ries, W. F., Lukovic, B., and Parker, R. N.: Landslides and ground damage caused by the Mw 7.1 Inangahua earthquake of May 1968 in northwest South Island, New Zealand, GNS Science, 89 pp., 2014.

Hancox, G. T., Ries, W. F., Parker, R. N., and Rosser, B.: Landslides caused by the MS 7.8 Murchison earthquake of 17 June 1929 in northwest South Island, New Zealand, GNS Science, 2016.

Heim, A.: Landslides & human lives = Bergsturz und Menschenleben, BiTech Publishers, Vancouver (BC, 1932.

Hicks, M., Shankar, U., McKerchar, A. I., Basher, L., Lynn, I., Page, M., and Jessen, M.: Suspended sediment yields from New Zealand rivers, J. Hydrol., 50, 81–142, 2011.

Hicks, M., Semadeni-Davies, A., Haddadchi, A., Shankar, U., and Plew, D.: Updated sediment load estimator for New Zealand, National Institute of Water & Atmospheric Research Ltd, 190 pp., 2019.

Horton, P., Jaboyedoff, M., Rudaz, B., and Zimmermann, M.: Flow-R, a model for susceptibility mapping of debris flows and other gravitational hazards at a regional scale, Nat. Hazards Earth Syst. Sci., 13, 869–885, 2013.

Hovius, N., Stark, C. P., and Allen, P. A.: Sediment flux from a mountain belt derived by landslide mapping, Geology, 25, 231–234, 1997.

Hutton, E., Barnhart, K., Hobley, D., Tucker, G., Nudurupati, S. S., Adams, J., Gasparini, N. M., Shobe, C., Strauch, R., Knuth, J., margauxmouchene, Lyons, N., DavidLitwin, Glade, R., Giuseppecipolla, Manaster, A., alangston, Thyng, K., and Rengers, F.: landlab/landlab: Mrs. Weasley, Zenodo, https://doi.org/10.5281/ZENODO.3776837, 2020.

Iovine, G., D'Ambrosio, D., and Di Gregorio, S.: Applying genetic algorithms for calibrating a hexagonal cellular automata model for the simulation of debris flows characterised by strong inertial effects, Geomorphology (Amst.), 66, 287–303, 2005.

Iverson, R. M. and Denlinger, R. P.: Flow of variably fluidized granular masses across three-dimensional terrain: 1. Coulomb mixture theory, J. Geophys. Res., 106, 537–552, 2001.

Jaboyedoff, M., Carrea, D., Derron, M.-H., Oppikofer, T., Penna, I. M., and Rudaz, B.: A review of methods used to estimate initial landslide failure surface depths and volumes, Eng. Geol., 267, 105478, 2020.

Jones, K. E., Howarth, J. D., Massey, C. I., Luković, B., Sirguey, P., Singeisen, C., Gasston, C., Morgenstern, R., and Ries, W.: An alternative to landslide volume-area scaling relationships: an ensemble approach adopting a difference model to estimate the total volume of landsliding triggered by the 2016 Kaikōura earthquake, New Zealand, Landslides, 22, 2219–2236, 2025.

Keck, J., Istanbulluoglu, E., Campforts, B., Tucker, G., and Horner-Devine, A.: A landslide runout model for sediment transport, landscape evolution, and hazard assessment applications, Earth Surf. Dyn., 12, 1165–1191, 2024.

Klar, A., Aharonov, E., Kalderon-Asael, B., and Katz, O.: Analytical and observational relations between landslide volume and surface area, J. Geophys. Res., 116, https://doi.org/10.1029/2009jf001604, 2011.

Lancaster, S. T., Hayes, S. K., and Grant, G. E.: Effects of wood on debris flow runout in small mountain watersheds, Water Resources Research, 39, https://doi.org/10.1029/2001WR001227, 2003.

Larsen, I. J. and Montgomery, D. R.: Landslide erosion coupled to tectonics and river incision, Nat. Geosci., 5, 468, 2012.

Larsen, I. J., Montgomery, D. R., and Korup, O.: Landslide erosion controlled by hillslope material, Nat. Geosci., 3, 247–251, 2010.

Lee, M. E. and Jones, D. K. C.: Landslide risk assessment, 3rd ed., ICE Publishing, London, England, 2023.

Leith, K. and Wichmann, V.: Landslide debris inundation risk and uncertainty from a process-based hazard model for the West Coast region of New Zealand, Submitted to Nat. Hazards Earth Syst. Sci., 2026.

Leith, K., McColl, S., Robinson, T., Massey, C., Smith, H., Wotherspoon, L., Carey-Smith, T., Ashraf, S., Barrell, D., Betts, H., Bidmead, J., Boyes, A. F., Bruce, Z., Buxton, R., Daysh, I., Dreyer, L., Easterbrook-Clarke, L., Farr, J., Glassey, P., Gnesko, L., Harvey, J., Heron, D., Hill, M., Jaramillo, A., Jones, K., Knoltsch, A., Lawson, R., Lee, J., Lin, A., Lukovic, B., Lyford, H., Pelmard, J., Pola, A., Rosser, B., Rozmus, K., Tamang, N. B., Townsend, D., de Vilder, S., Wight, J., Wolter, A., Zhao, H., and Zoeller, A.: Cyclone Gabrielle (12–16 February 2023): Landslide inventory for North Island New Zealand, version 1.0, Earth Sciences New Zealand, 2025a.

Leith, K. J., de Vilder, S. J., Massey, C. I., and Lukovic, B.: Regional landslide-debris-inundation analysis for West Coast Emergency Management, GNS Science, Lower Hutt, NZ, 146 pp., 2025b.

Lin, A. F., Zorn, C., Wotherspoon, L., Robinson, T. R., and Pelmard, J.: Prediction of road blockages caused by rainfall-induced landslides, N. Z. J. Geol. Geophys., 68, 983–999, 2025.

LINZ: NZ 8m Digital Elevation Model (2012), 2012.

Liu, J., Wu, Y., Gao, X., and Zhang, X.: A simple method of mapping landslides runout zones considering kinematic uncertainties, Remote Sens. (Basel), 14, 668, 2022.

Massey, C. I., de Vilder, S. J., Lukovic, D. B., Townsend, B., and Rosser, B. J.: District-scale landslide risk analysis of debris inundation for the Kaikōura District, GNS Science, Lower Hutt, New Zealand, 117 pp., 2020a.

Massey, C. I., Townsend, D. T., Lukovic, B., Morgenstern, R., Jones, K., Rosser, B., and de Vilder, S.: Landslides triggered by the MW7.8 14 November 2016 Kaikōura earthquake: an update, Landslides, https://doi.org/10.1007/s10346-020-01439-x, 2020b.

Massey, C. I., Townsend, D., Jones, K., Lukovic, B., Rhoades, D., Morgenstern, R., Rosser, B., Ries, W., Howarth, J., Hamling, I., Petley, D., Clark, M., Wartman, J., Litchfield, N., and Olsen, M.: Volume Characteristics of Landslides Triggered by the MW 7.8 2016 Kaikōura Earthquake, New Zealand, Derived From Digital Surface Difference Modeling, Journal of Geophysical Research: Earth Surface, 125, e2019JF005163, 2020c.

McDougall, S.: 2014 Canadian Geotechnical Colloquium: Landslide runout analysis — current practice and challenges, Can. Geotech. J., 54, 605–620, 2017.

McDougall, S. and Hungr, O.: A model for the analysis of rapid landslide motion across three-dimensional terrain, Can. Geotech. J., 41, 1084–1097, 2004.

Medina, V., Hürlimann, M., and Bateman, A.: Application of FLATModel, a 2D finite volume code, to debris flows in the northeastern part of the Iberian Peninsula, Landslides, 5, 127–142, 2008.

Medwedeff, W. G., Clark, M. K., Zekkos, D., and West, A. J.: Characteristic landslide distributions: An investigation of landscape controls on landslide size, Earth Planet. Sci. Lett., 539, 116203, 2020.

Mergili, M., Fellin, W., Moreiras, S. M., and Stötter, J.: Simulation of debris flows in the Central Andes based on Open Source GIS: possibilities, limitations, and parameter sensitivity, Nat. Hazards, 61, 1051–1081, 2012.

Mishra, A. K., Placzek, C., and Jones, R.: Coupled influence of precipitation and vegetation on millennial-scale erosion rates derived from 10Be, PLoS One, 14, e0211325, 2019.

Montgomery, D. R. and Brandon, M. T.: Topographic controls on erosion rates in tectonically active mountain ranges, Earth Planet. Sci. Lett., 201, 481–489, 2002.

Moreno, M., Steger, S., Tanyas, H., and Lombardo, L.: Modeling the area of co-seismic landslides via data-driven models: The Kaikōura example, Eng. Geol., 320, 107121, 2023.

Murray, A. B.: Reducing model complexity for explanation and prediction, Geomorphology (Amst.), 90, 178–191, 2007.

Neverman, A. J., Donovan, M., Smith, H. G., Ausseil, A.-G., and Zammit, C.: Climate change impacts on erosion and suspended sediment loads in New Zealand, Geomorphology, 427, 108607, 2023.

NIWA Taihoro Nukurangi: HIRDS v4 Rainfall Depth Surfaces New Zealand, 2022.

Perla, R., Cheng, T. T., and McClung, D. M.: A Two–Parameter Model of Snow–Avalanche Motion, J. Glaciol., 26, 197–207, 1980.

Pollock, W.: A Framework for Regional Scale Quantitative Landslide Risk Analysis, 2020.

Pollock, W. and Wartman, J.: MM3: Multimodal framework for regional-scale quantitative landslide risk analysis, MethodsX, 14, 103218, 2025.

Pollock, W. and Wartman, J.: Disaggregation of landslide risk, Earths Future, 14, e2025EF007594, 2026.

Pollock, W., Grant, A., Wartman, J., and Abou-Jaoude, G.: Multimodal method for landslide risk analysis, MethodsX, 6, 827–836, 2019.

Prajapati, G. and Jaboyedoff, M.: Method to estimate the initial landslide failure surface and volumes using grid points and spline curves in MATLAB, Landslides, 19, 2997–3008, 2022.

Pudasaini, S. P. and Krautblatter, M.: The mechanics of landslide mobility with erosion, Nat. Commun., 12, 6793, 2021.

Read, S. A., Perrin, N. D., Richards, L. R., and Others: Applicability of the Hoek-Brown failure criterion to New Zealand greywacke rocks, in: 9th ISRM Congress, 1999.

Reid, M. E., Coe, J. A., and Brien, D. L.: Forecasting inundation from debris flows that grow volumetrically during travel, with application to the Oregon Coast Range, USA, Geomorphology , 273, 396–411, 2016.

Roda-Boluda, D. C., Schildgen, T. F., Wittmann, H., Tofelde, S., Bufe, A., Prancevic, J., and Hovius, N.: Elevation-dependent periglacial and paraglacial processes modulate tectonically-controlled erosion of the Western Southern Alps, New Zealand, J. Geophys. Res. Earth Surf., 128, https://doi.org/10.1029/2023jf007271, 2023.

Santangelo, M., Marchesini, I., Bucci, F., Cardinali, M., Cavalli, M., Crema, S., Marchi, L., Alvioli, M., and Guzzetti, F.: Exposure to landslides in rural areas in Central Italy, J. Maps, 17, 124–132, 2021.

Schaller, M. and Ehlers, T. A.: Comparison of soil production, chemical weathering, and physical erosion rates along a climate and ecological gradient (Chile) to global observations, Earth Surf. Dyn., 10, 131–150, 2022.

Tenzer, R., Sirguey, P., Rattenbury, M., and Nicolson, J.: A digital rock density map of New Zealand, Comput. Geosci., 37, 1181–1191, 2011.

de Vilder, S., Massey, C., Lukovic, B., Taig, T., and Morgenstern, R.: What drives landslide risk? Disaggregating risk analyses, an example from the Franz Josef Glacier and Fox Glacier valleys, New Zealand, Nat. Hazards Earth Syst. Sci., 22, 2289–2316, 2022.

Whittall, J.: Runout estimates and risk-informed decision making for bench scale open pit slope failures, Can. Geotech. J., 57, 1044–1057, 2020.

Wichmann, V.: The Gravitational Process Path (GPP) model (v1.0) – a GIS-based simulation framework for gravitational processes, https://doi.org/10.5194/gmd-10-3309-2017, 2017.